PCCP

Accepted Manuscript

ROYAL SOCIETY OF CHEMISTRY

www.rsc.org/pccp

PCCP

RSCPublishing

PERSPECTIVE

Indentation-formed nanocontacts: An atomic-scale perspective

Cite this: DOI: 10.1039/x0xx00000x

William Paul,[a,b] David Oliver,[a] and Peter Grütter[a]

Received 00th January 2012,
Accepted 00th January 2012

DOI: 10.1039/x0xx00000x

www.rsc.org/pccp

One-to-one comparisons between indentation experiments and atomistic modelling have until recently been hampered by the discrepancy in length scales of the two approaches. Here, we review progress in atomic-scale nanoindentation experiments employing scanning probe techniques to achieve depth-sensing indentation and field ion microscopy to permit detailed indenter characterization. This perspective addresses both mechanical (dislocation nucleation, defect structures, adhesion, indenter effects) and electronic (interface, disorder, and vacancy scattering) properties of indentation-formed contacts.

Table of contents

1. Introduction

Indentation is an important mechanical test which has found spectacular use from the characterization of nanocomposite materials [1, 2] to mapping the mechanical properties of biological materials such as dental enamel [3]. During indentation testing, the applied load is recorded as a function of indentation depth [4-7]. Force-displacement curves, though relatively simple to obtain, are challenging to interpret at a fundamental level due to the complex stress distribution within the specimen. Therefore in order to understand deformation mechanics at the atomic scale and to interpret the features of experimental data, atomistic simulations are needed to 'look inside' materials while an indentation stress is applied [8].

Compared with experiments, computer simulations are much cleaner (surfaces are free of ambient water layers and hydrocarbons), much faster (of the order $10^9\times$), and are carried out between materials of perfect atomic composition. The substantial mismatch in length scales is an additional hindrance in relating experimental results with those from simulations – molecular dynamics can handle up to some millions of atoms (lateral size and depth of tens of nm), but traditional nanoindentation testing will involve at the very minimum ~10^{10} atoms (μm lateral size and tens to hundreds of nm depth).

The interdependency of experiments and simulations/theory has proven to be an important theme in the history of science [9]. Because models are so valuable to our understanding of

experiments, it is important to be able to test their correctness – this "validation" relies on experimental results with as many parameters matched to the models as possible. With both approaches generating cutting-edge observations and open questions, we hope that efforts to close the length scale gap will ignite future collaborations. This has certainly been the case for atomic-scale friction, where comparisons between friction force microscopy experiments and molecular dynamics simulations have become quite commonplace: A recent issue of Tribology Letters was in fact devoted to "Combining Experiment and Theory in Tribology" [10].

Matching length scales to molecular dynamics simulations is experimentally challenging: It requires characterizing nanometer-size indenters, measuring nanonewton forces, and imaging residual impressions with nanometer resolution. In this article, we focus on recent experimental progress in closing this length scale gap, particularly in the application of scanning probe microscopy (SPM) to indentation. We also emphasize experimental methods which allow for the full 3D atomic structure of the indenter to be determined, namely by field ion microscopy (FIM).

The outline of this article is as follows: In Section 2, the development of nanoindentation tools is reviewed, and we present a SPM-based approach to experimentally realize atomic-scale indentation. Indenter preparation and characterization by FIM is also described.

Mechanical properties of nanocontacts are presented in Section 3, starting with a review of dislocation nucleation in atomic-scale indentation systems. We address phenomena which are unique to indentation at this length scale which have been identified in simulations and experiments: Effects of atomically rough indenters, defects structures in residual impressions, temporal evolution, adhesion, tip wetting, and the threshold for incipient plasticity.

Section 4 focuses on electron transport through indentation nanocontacts. We discuss ballistic transport in related break-junction type contacts, and then describe the distinguishing characteristics of electron transport through an indentation contact. Namely, interfaces between dissimilar materials and defect structures within substrates contribute to significant additional resistance, the magnitude of which was unanticipated. These results are important to our understanding of how to establish reliable interfaces between macroscopic electric circuits and nanoscale structures.

We provide an outlook for future experiments and modelling work in Section 5.

2. Experimental methods

Indentation can be a relatively simple mechanical test to characterize material properties, particularly hardness, and has been used for this purpose for over a century [11]. Hardness refers to a material's resistance to plastic deformation, and as a material property, its definition is problematic because the yield point depends on the volume being probed, the indenter geometry, etc. In a most straightforward indentation measurement, hardness corresponds to the force per area supported by the material during fully developed plastic deformation. For years, the contact area had been extracted by examination of the residual impression by optical microscopy post-indentation, and the hardness obtained as $H = P/A$, where P is the applied load, and A the projected (cross-sectional) contact area.

A desire to shrink the length scales of indentation was motivated by the prospect of probing the mechanical properties of just *one* crystalline grain of a material at a time as well as that of mapping local properties across specimens. A major hurdle in shrinking the indentation size was the accurate determination of contact area after unloading (often too small to be resolved by optical microscopy). This prompted the development of depth-sensing instrumentation in the 1980s, where the load and penetration depth are both recorded during indentation [12-14].

A typical nanoindenter is composed of a force actuator (e.g. inductive coil) and displacement sensor (e.g. capacitive) to apply a programmed load vs. time or displacement vs. time profile to the specimen under test by way of a hard tip (usually diamond) [4, 12, 15]. Most often, the shape of the indenter tip is a three-sided Berkovich pyramid whose geometric self-similarity creates a simple relationship between indentation depth and contact area. The force and displacement data acquired during the test are plotted in a load-displacement curve (also known as force-distance or *P-h* curve). The overall shape of the load-displacement curve reflects the mechanical properties of the material being probed, and quantitative properties can be extracted using the known indenter geometry.

The acquisition of the entire force-displacement profile in depth-sensing indentation allows the nanoindenter to measure not only hardness, but also elastic modulus, strain-hardening exponents, fracture toughness, and viscoelastic properties. Time-dependent indentation response can also be measured by holding the indenter at maximum load (creep testing), or by applying a modulated load to extract the complex elastic modulus (storage and loss components) [16, 17]. Time-dependent techniques are very important to the characterization of polymers [18] and biological materials [19, 20]. We note that in contrast to viscoelastic materials, the metal nanocontacts considered in this article deform in a purely elastic-plastic manner (however thermal activation does add temporal dependence to discrete plastic events, Section 3.4).

The large mismatch in length scales between traditional nanoindentation and atomistic simulations motivates us to look for new ways to experimentally investigate indentation response. To create the opportunity for a one-to-one spatially matched comparison, innovations in several key areas are essential: Firstly, the resolution of applied loads must be improved below the several hundred nN baseline typical of nanoindenters. Experiments carried out inside a transmission electron microscope have shown that the initial yield events can occur at very low loads near or below the resolution limit [21]. The application of atomic force microscopy to nanoindentation, first considered to enable smaller indenter displacements [22],

now permits the resolution of pop-in events down to the nN regime [23, 24]. However, tip characterization, depth determination and calibration accuracy can be challenging.

Secondly, one must have good experimental control over surface chemistry which governs mechanics at the interface, notably adhesion [25]. Carrying out the experiment and the preparation of the sample and tip surfaces in ultra-high vacuum allows the contact to be made between clean metal surfaces.

Finally, indenter characterization becomes increasingly difficult as the length scale of interest decreases. Ultimately, one must determine not only the indenter radius, but also the crystallographic direction of the apex and the structure of the stepped crystal surface. Apex characterization can be carried out by scanning and transmission electron microscopy (usually *ex situ*) [26, 27], but these techniques cannot determine the full 3-D structure at the atomic scale.

In the sections that follow, we describe a SPM-based approach to atomic-scale nanoindentation using a cantilevered sample whose deflection is monitored by optical interferometry. We then describe the preparation of clean tungsten indenters and their characterization at the atomic scale by FIM.

2.1 Indentation by Scanning Probe Microscopy

Scanning tunneling microscopy (STM) and atomic force microscopy (AFM) are common variants of SPM, both of which can be used to create and image indentation structures at the atomic scale. In this section, the operating principles of STM and AFM are first overviewed, then particular applications to indentation are addressed.

In STM, a small electric current tunneling between the tip and the sample, on the order of pA to nA, is used as an imaging mechanism [28-30]. Due to the current's exponential dependence on the tip-sample distance, with one decade of variation per Ångström, excellent spatial resolution is possible (however its application is limited to conducting samples). In AFM, the force or force gradient between the tip and sample is responsible for image contrast [31, 32]. Electrostatic, van der Waals, and chemical bonding forces all contribute to the force-distance profile, so the AFM's resolution depends on which particular force interaction is dominant. STM and AFM imaging is carried out by raster scanning the tip over the sample while under feedback to maintain either constant tip-sample current (STM) or force (AFM). This procedure traces out an isosurface of constant tip-sample interaction, often termed the 'topography' of the sample.

SPM can also be used to perform spectroscopy, in which the feedback loop is broken and one experimental parameter is varied and the response of another is measured, such as force vs. distance, current vs. distance, current vs. voltage etc. Nanoindentation carried out by SPM can be considered as a type of force-distance spectroscopy.

Using force (AFM) or current (STM) feedback for imaging, valuable information about dislocation structures can be obtained with high spatial resolution: Dislocation configurations such as 'mesas' (a small surface protrusion caused by two pairs of Schockley partial dislocations) and 'screw-loops' (half-loops with screw component intersecting the surface) have been investigated on the Au(100) surface in atomic detail by STM [33-37]. Surface imaging is often done in contact mode under a repulsive force of several hundred nN [22, 38], but recent studies have reported the use of noncontact mode imaging with the same cantilever and tip used for indentation [39].

In SPM-based indentation, tip actuation is almost always provided by a piezoelectric crystal, which allows exceptional force and depth control, but is susceptible to hysteresis and creep. Several commercial instruments operating in ambient conditions (i.e. room temperature, atmospheric pressure) allow 'closed loop' indentation to be carried out in which hysteresis and creep are compensated by feedback to allow the true force and depth to be measured. For AFMs operating under UHV conditions, closed-loop scanners are rare due to the added instrumentation complexity [40].

Due to the obstacles of hysteresis and creep, as well as the added analysis step of correcting for the bending of the cantilever, many previous UHV studies have neglected to obtain the true depth of indentation. Nonetheless, UHV AFM studies have provided important insight into atomic-scale discrete plastic phenomena such as pop-ins and dislocation structures [24, 26, 41]. Other imaging modes based on AFM can also be implemented, such as Kelvin Probe Force Microscopy (KPFM) to map the local charge distribution around defect structures in ionic crystals [27].

Closely related to the AFM is the interfacial force microscope (IFM) which employs feedback to maintain an effective infinite stiffness between the tip and the surface, rather than the finite compliance of an AFM cantilever [38, 42].

2.1.1 Cantilever beam technique. Our interest lies in the use of atomically characterized indenters, carried out by *in situ* FIM preparation and characterization. To do this, the tip must be made of a material compatible with the large electric fields required for FIM operation which rules out the use of traditional microfabricated silicon cantilevers as force sensors. Our SPM implementation can be considered as a STM supplemented with a force sensor: The tip is rigidly mounted like that of a STM and the sample is constructed as a cantilever so that it can deflect upon interaction with the tip. Interferometry returns quantitative displacements of the beam, calibrated directly to the wavelength of light.

In a combined STM/AFM indentation, the electric current through the tip-sample junction will vary by many orders of magnitude in a typical measurement, passing from the quantum-mechanical tunneling to contact regimes. Therefore in order to perform tunneling measurements (i.e. STM) and to probe the electrical properties of a fully-developed contact, it is necessary to accurately measure current across a very high dynamic range (pA-mA). This is achievable with the use of a logarithmic amplifier [43].

Restricting indentation to depths of the order of a few nanometers causes minimimal hysteresis and creep in the piezotube and permits accurate depth measurements to be obtained. This low displacement regime is inherently

interesting as the regime where the initial onset of plasticity in pristine materials can be observed [44]. Very sharp indenters (radii of ~12 nm or less) are necessary to operate in this regime. Such sharp indenters are also convenient for FIM, because blunter tips require higher applied voltages (which are already ~10 kV for a 12 nm tip).

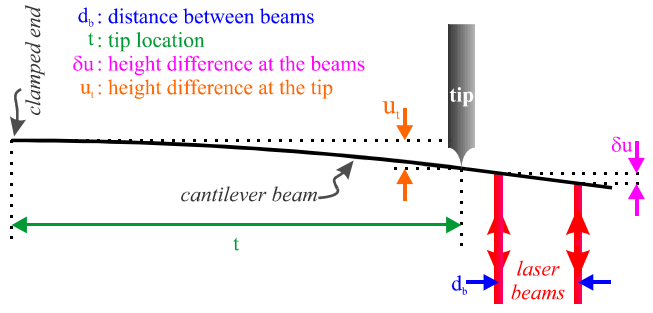

Figure 1: Cantilever beam, tip, and laser interferometer geometry illustrating important measurement quantities. The distance between the interferometer beams, d_b, is 1 mm in our setup. The typical size of such a cantilever beam is 5 mm × 1 mm × 50 µm. The spring constant is 80-200 N/m at the measurement location. The resonance frequency the beam is ~ 2 kHz. Detailed derivations of these quantities are given elsewhere [45, 46].

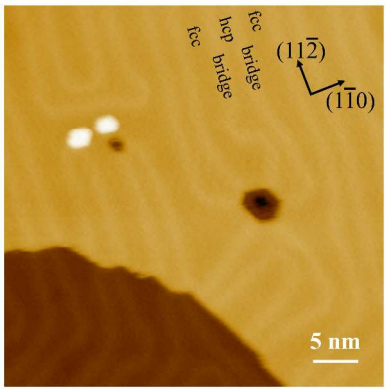

Figure 2: Constant current topographic STM image of the Au(111) surface on a Au/mica cantilever beam taken at 8pA, -0.9V sample bias. One atomic step of height 0.236 nm occurs in the bottom-left part of the image. Two indentations with the STM tip have been carried out; the resulting hexagonal holes reflect the symmetry of the surface atoms. Surrounding the top-left hole are two islands of single atomic layer high Au pileup which resulted from indentation. The Au(111) surface reconstructs into a 22 × $\sqrt{3}$ surface unit cell which accommodates 23 atoms in 22 surface sites along the $(1\bar{1}0)$ direction [47, 48]. The raised bridge sites give rise to small topographic variations within atomically flat terraces, labeled 'bridge.' Regions of fcc, hcp, and bridge site stacking are identified on the surface reconstruction's discommensuration lines.

Figure 1 illustrates the setup of the cantilevered sample and STM tip indenter. The tip applies a point load to the cantilevered sample at a distance t from the clamping point. The load and deflection of the beam at the location of the tip are derived from the slope of the beam on the free end (where the slope is constant) measured by interferometry. The interferometer in our setup measures the phase difference between to beams with orthogonal polarization which are reflected from the sample. The design of such an interferometer is described elsewhere [49]. This Nomarski-type interferometer is well suited to the measurement of slow cantilever deflections because its output is unaffected by low frequency laser intensity noise: the interferometer signal is obtained by subtraction of two photodiode signals, resulting in good common-mode rejection.

The cantilevered sample must perform simultaneously as a surface-science quality substrate and as a sensitive force transducer. We have found a highly successful sample configuration to consist of Au(111) surfaces made by double-sided thermal evaporation of Au on freshly cleaved muscovite mica (Axim grade V-1) to a thickness of 100 nm. Complete fabrication details can be found in Ref. [45]. The thickness of thin-film samples should be at least five times the indentation depth so that stress fields are well contained within the thickness of the sample [50]. Indentation depths are typically less than 3 nm, ensuring that measurements on these films reflect the same properties as bulk crystals.

Final surface preparation is carried out in UHV before indentation experiments by cycles of 1keV Ne+ ion bombardment and annealing to ~400 °C. A topographic STM image of a clean Au(111) surface with two indentation-produced holes is shown in Figure 2.

The mica beam technique is in principle extensible to single-crystal Ag(111), Cu(111), Al(111) and Pt(111) substrates prepared by thermal evaporation [51-53]. Metal films on mica are limited to the close-packed (111) direction, so other crystallographic orientations would require fabrication of beams from bulk single crystals. We have recently explored the bulk single crystal method, and have fabricated a 100 µm thick Cu(100) cantilevered sample by careful grinding and lapping [45]. Another approach is to decouple the force transduction from the surface-science substrate by affixing a small crystal of interest to a gold-on-mica or gold-on-glass cantilever beam. We have performed nanoindentation on a 1 mm × 1 mm × 0.45 mm InSb(001) crystal in this manner [45]. The major limitation to the affixed-sample technique is the substantial decrease in cantilever beam resonance frequency due to mass loading, resulting in greater coupling of mechanical noise into the tip-sample junction.

Isolation of the experiment from mechanical vibrations and thermal drift is a common concern in both indentation and scanning probe work. For a STM to work at all, mechanical vibrations must be kept well below 1 Å or else a stable tunneling current would not be achievable (the tunnel current varies by one order of magnitude per Ångström of separation). Various solutions for vibration isolation have been discussed in the SPM literature [54-57]. In our lab, vibration isolation is achieved by passive means of suspending the entire UHV chamber from bungee cords with an extension length of 1 m, yielding a cutoff frequency of 0.5 Hz. The SPM is also suspended inside the vacuum chamber from bellows for an additional isolation [58]. Thermal drift is below 1 Å between the start and end of the indentations carried out on the 1-2

second timescale and is not corrected in these experiments. If necessary, it can be compensated by a linear feed-forward feature of the SPM controller [59].

2.1.2 Discrete plasticity and control methods. Plastic processes are often detected as discretized 'pop-ins' in nanoindentation [5, 7]. Pop-ins can arise from the nucleation of dislocations, the initiation of a glide process, or a phase transformation due to the applied stress (in the case of some semiconductors [60, 61]).

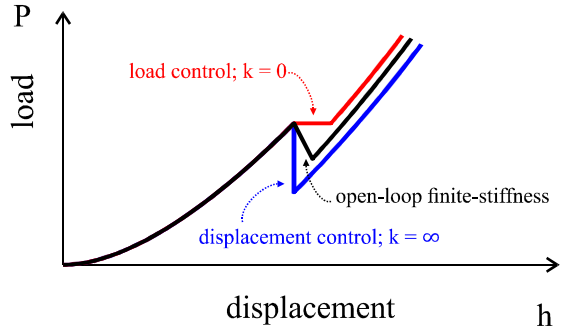

Figure 3: Control methods for nanoindentation showing the appearance of discrete plastic events as either a sudden displacement excursion (load control, red), a drop in load (displacement control, blue), or a simultaneous drop in load and increase in penetration depth (open-loop finite-stiffness, black).

A point worth appreciating is that the pop-in appears differently in load-displacement curves depending on the control method employed. Most nanoindentation tests are performed under load control, where the load is increased under feedback at a constant rate. When a pop-in occurs, the same load will be maintained while the indenter travels suddenly into the material. This scenario corresponds to an effective zero stiffness between indenter and sample and is depicted by the horizontal discontinuity in Figure 3. Load control is somewhat alarming from a physical perspective: After the pop-in, the contact is immediately re-loaded, possibly concealing further plastic processes which would have occurred at lower loads while re-loading the contact [62].

An ideal apparatus would maintain an infinite stiffness between indenter and substrate, allowing the pop-in to unload the contact without having the indenter penetrate further into it. This displacement controlled scenario is illustrated by the vertical discontinuity in Figure 3, and can be achieved experimentally in the IFM [63], as well as some commercial nanoindenters [62].

In AFM-based indentation, the cantilever imparts a finite stiffness between the indenter and substrate. In the absence of feedback control, the pop-in will appear as a simultaneous drop in force and an increase in penetration depth. The slope of the pop-in is the compliance of the force transducer which links forces to tip-sample displacements. This type of pop-in is shown in Figure 3 by the sloped discontinuity. We refer to this indentation mode as 'open-loop finite-stiffness'.

2.1.3 Nanoindentation response at the atomic scale. We now introduce some typical features of an atomic-scale indentation curve using Figure 4 as an example. The zero point of the indentation depth, indicated by A, is set to the crossing of the 1 GΩ tunneling point of the conductance data. Note that this is a semi-arbitrary zero, since at these scales there is no unambiguous definition of the exact point of contact. A jump-to-contact is observed in the current at point B where the conductance of the junction suddenly jumps to ~ 3 G_0. Pop-ins are observed at the points labeled C on the loading force curve (not all pop-ins are circled). At ~50 nN on the unloading force curve, a pop-out is observed at point D, interpreted as a discrete event which partially reverses plasticity created during loading of the contact. The large adhesion of the metallic contact is observed at E. Upon unloading, the conductance trace (red) shows a large hysteresis, indicating that a wire is drawn which finally breaks at point F at a conductance of just over 1 G_0. If the drawn atomic wire is sufficiently short, sometimes a tunneling current is measured after its breaking. In the example shown, no tunneling behaviour is present – the slow decay toward the detection baseline, labeled G, is due to the long settling time of the logarithmic current preamplifier in the low current regime.

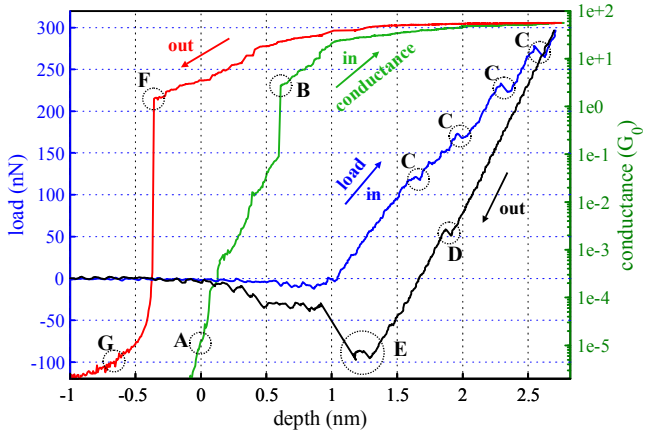

Figure 4: A load-displacement curve showing several important features of atomic-scale nanoindentation experiments (see text). On the loading (in) curve, load is blue and conductance is green. On the unloading (out) curve, load is black and conductance is red.

2.2 Indenter characterization and preparation by Field Ion Microscopy

Indenters are most commonly made of diamond, tungsten carbide, or other hard materials so that impressions can be made in test specimens without the tips undergoing plastic deformation themselves. Tungsten happens to be one of the most routinely studied metals in FIM: Because of its strong covalent bonds [64], it can withstand the high electric fields needed for FIM. Tungsten's strong bonding also makes it a very hard metal, ensuring that plastic damage happens only within the indented substrate. Post-indentation, a gold wetting

layer can be removed by field-evaporated in FIM to recover a tip with identical radius. In exceptional cases of unintended tip crashing, dislocations in the tip can be imaged by FIM [46].

FIM is historically notable as the earliest technique to have produced real-space images of matter with atomic resolution [65-67]. It is a particularly simple form of microscopy compared to the complexities of electron optics in SEM or TEM, or the control systems and vibration isolation required for SPM. FIM requires just a sample in the form of a sharp tip, a phosphor screen at a distance of ~10 cm from the tip, a vacuum system backfilled with ~10^{-5} mbar of He (or other appropriate imaging gas), and a high voltage supply. During operation, the high positive voltage applied to the tip will create large enough electric fields to ionize He atoms near its apex, around 4.4 V/Å, which are then detected on a phosphor screen.

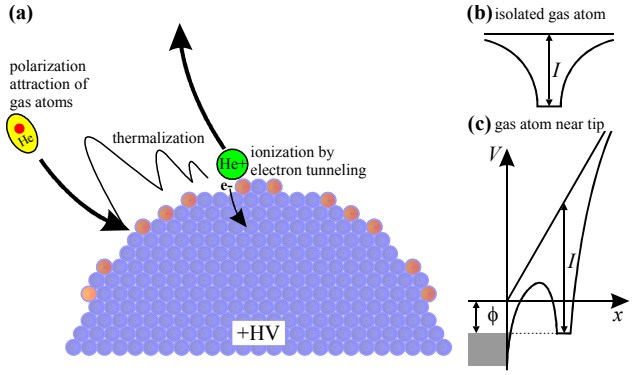

Figure 5: (a) Side view of a tip apex showing the dipole attraction of imaging gas atoms, thermal accommodation to the tip, and ionization over an atomic site of locally enhanced field (orange). (b) Potential energy diagram of a valence electron in a gas atom. (b) Potential energy diagram when the atom is within tunneling distance of the metal tip and subjected to a large electric field.

The process of field ionization is detailed in Figure 5. The dipole attraction of gas atoms occurs near the apex in the presence of the strong field. If the tip is cooled, the gas atoms will thermalize to the tip as they hop over its surface – this contributes to a lower initial random thermal velocity when the gas atom ionizes and improves resolution. The He gas atom has the highest probability of being ionized over a protruding atom where the field is locally enhanced, such as those indicated in orange.

The loss of an electron from the gas atom to the tip happens by quantum mechanical tunneling. The potential energy landscape of a valence electron in a gas atom with ionization energy I is shown in Figure 5 (b). In an applied field, the potential becomes sloped. When brought sufficiently close to a metal tip, as illustrated by Figure 5 (c), the potential barrier between the electron state in the gas atom and an available electron state in the tip becomes small enough to permit tunneling with reasonable probability.

Once ionized, the He^+ ion is accelerated by the field toward a microchannel plate and phosphor screen for detection. The image on the screen reflects the spatial distribution the imaging gas ionization rate and thus gives atomically resolved information regarding the tip shape. The atomically-resolved image of the tip apex can be captured by a camera, or even admired by the naked eye.

FIM images of tungsten tips with (110) and (111) oriented apices are shown with the low index planes labelled in Figure 6.

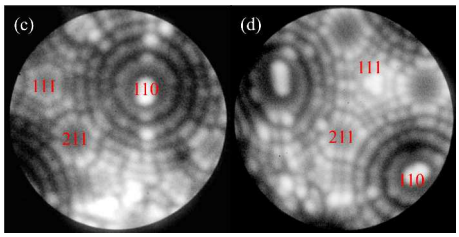

Figure 6: (a) W(110) (b) W(111) tips with low index planes identified. Atoms on the (111) planes are individually resolved, while only the step edges of the smooth (110) planes are imaged. The crystallographic axes of the tips are offset from the center due to electrostatic distortion of the image.

2.2.1 FIM and SPM. Several groups have put significant effort toward the marriage of FIM and SPM techniques over the last three decades [57, 68-75]. Notable to the subject of nanocontacts is the work of Manfred Leisch's group which was distinctly motivated by the prospect of making well-controlled contacts between FIM tips and surface-science quality substrates using STM [76, 77]. This was essentially an experimental realization of the metal contacts studied in atomistic simulations [78] (although without force detection). The experimental investigation of mechanical interactions between tips defined in FIM and other specimens was not completely new – this had been investigated to some extent in the 1960s and 70s by Müller and Nishikawa [79], but the lack of control over interaction forces between the tip and contacting specimen made it difficult to avoid destroying the delicate FIM tip. Leisch's group identified that the techniques developed for SPM (e.g. piezoelectric transducers, vibration isolation, tip regulation feedback methods) were ideal for controlling mechanical interactions with FIM tips at atomic length scales. Using STM control of the tip and a time-of-flight mass spectrometer incorporated into the FIM, the number of atoms transferred from the substrate to the tip during indentation could be counted. The authors also made interesting observations regarding changes to the tip structure induced during STM imaging [77].

2.2.2 Tungsten tip etching. Sharp tungsten tips are etched by electrochemical etching at 3 V_{DC} in a 9.85 mol/l KOH solution, detailed in Ref [80], and along the lines of standard recipes found in the STM literature [81-83]. Further information on field emission and characterization of these tips can be found in Refs. [84, 85].

2.2.3 Field evaporation in FIM. A pristine tungsten tip can be prepared by increasing the voltage during FIM imaging by about 10-20 % relative to the imaging voltage. The elevated voltage induces the process of field evaporation in which

surface atoms are ionized and removed under the high electric field. Field evaporation is used to remove transferred layers of substrate material between sets of indentation experiments as well as adsorbed rest gases after prolonged storage in UHV. This process guarantees that the surface of the tip consists only of tungsten atoms.

2.2.4 Tip integrity. Recently, we have developed a 'force field' protocol to ensure that the atomic structure of FIM tips is maintained in the transfer processes between FIM and SPM modes [86]. Due to the high reactivity of tungsten, rest gases in UHV and impurity gases present during FIM imaging can chemically bind to the tip surface and modify its atomic structure and surface chemistry; it is therefore crucial to ensure good UHV conditions and prompt transfer between FIM and SPM. Briefly, the 'force field' protocol uses a high applied voltage to the tip to ionize impinging gas atoms before they can react with the tip apex, guaranteeing that a clean tungsten tip can be used for the SPM experiment. This is especially useful if processes which induce pressure transients must be performed during sample transfer, etc. The rate of tip degradation in a UHV environment due to the statistical arrival of rest gases has been discussed in detail in [86]; it is reasonable to conduct an experiment with only some tens of atomic changes to a tungsten tip over an area of 120 nm^2.

2.2.5 Radius determination. The radius of curvature at the apex of FIM tips can be obtained by the ring counting method. The ring counting method can be described as follows [66]: Assuming a spherical envelope of the tip apex, the local radius of curvature, R, between two crystallographic poles separated by angle θ can be found by counting the number of visible rings, n, between them. Using the interlayer spacing, s, corresponding to the appropriate crystal plane, the radius can be written as $R = ns/(1-\cos\theta)$. This equation describes the geometry illustrated in Figure 7.

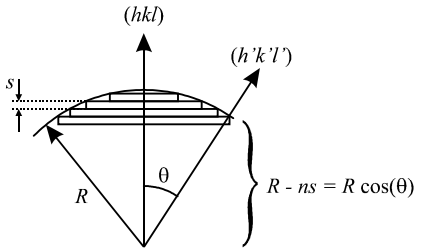

Figure 7: Side view of a tip with radius R showing the geometry of ring counting. Planes with spacing *s* are normal to the *(hkl)* direction, and *n* steps of height *s* are counted from pole *(hkl)* to *(h'k'l')*.

For ring counting estimations to be accurate, each counted ring must correspond to a *single* atomic step of type *(hkl)*. Often, however, a single 'ring' visible in a FIM image can correspond to multiple atomic planes of height *s*: Counting FIM rings is not equivalent to counting steps, as we describe in Refs. [86, 87]. These concerns have also appeared in work by Webber on the detailed determination of tip shape from FIM micrographs [88, 89]. Within the spherical region of the tip, the radius can be determined between various pairs of crystallographic poles to ± 0.5 rings, which corresponds to an uncertainty of ~ 0.6 nm.

2.3 Modelling

Of the various modelling approaches suitable to indentation, molecular dynamics (MD) is the most relevant at the length scales of interest here. MD allows the investigation of the time evolution of atomic ensembles ranging in size up to millions of atoms, overlapping with the nanometer scales recently achieved by AFM-based nanoindentation methods.

Continuum modelling approaches have been extensively studied in the context of traditional nanoindentation [12-14, 90, 91]. Even at nanometer scales, continuum indentation models retain some utility, particularly as an approximation of the elastic response of the material. In order to investigate mechanisms of plasticity at the single-event level, however, an atomistic approach such as MD is required.

Ab initio calculations of electronic transport can be carried out using density functional theory (DFT). This technique is highly computationally intensive, and experimentally accessible contact configurations are too large to directly simulate. Calculations on smaller model systems can nonetheless provide valuable insight.

2.3.1 Molecular dynamics. In MD, the time evolution of an ensemble of atoms is simulated by numerically solving the classical equations of motion for each atom over a series of time steps. The force on a given atom is given by a defined relationship known as a 'potential function.' A very wide range of atomic systems can be modelled with MD by selecting appropriate potential functions; furthermore, a wide range of physical situations can be investigated through the use of 'external' effects or constraints applied to the ensemble, such as an external force on the atoms.

Given initially defined positions and velocities for a set of atoms, and a potential function for calculating the force on any given atom as a function of the positions of its neighbouring atoms, numerical integration of Newton's equations of motion can be used to find the state of the system at any future time. One widely-used algorithm for this purpose is Verlet integration [92]. In order for the integrated system trajectory to converge to the 'true' trajectory, the integration time step used for MD must be kept short. Here 'short' is relative to the highest-frequency response of the system; 1 fs is a typical time step for metal-metal simulations. This tends to limit total simulation timespans to the ps-ns range, at least for atomic ensemble sizes relevant to indentation (thousands to millions of atoms).

In order to carry out an indentation 'experiment' in an MD simulation, the system must be externally actuated (externally, that is, relative to the natural dynamics of the isolated system) in some way so as to bring the indenter in contact with the substrate. One way to do this, assuming an atomically-defined indenter tip, is to advance the tip towards the substrate in small increments by moving a rigid layer of atoms at the base of the

tip. This corresponds to a 'displacement-controlled' indentation experiment, as discussed in 2.1.2. In fact it is more popular in the modelling literature to abstract the indenter away entirely, presumably to save the computational expense of computing the individual tip atoms. Instead, a spherical repulsive field is added to the system, and lowered into contact with the substrate (again, in a displacement-controlled fashion). This is effectively equivalent to using a smooth, hard-sphere indenter.

The potential function governs the atomic interactions in a MD simulation. Various styles of potential are available, with the choice primarily determined by the character of the material under investigation. The embedded-atom method (EAM), a potential style which incorporates many-body effects by 'embedding' the atoms in an electron cloud made up of contributions from neighbouring atoms, is appropriate for modelling many metallic species [93]. For covalently-bonded materials, a function which incorporates bond-angle dependence (a three-body effect) is necessary, such as the Stillinger-Weber potential [94]. Many other potential types have been developed to deal with different materials and material combinations [92]. Once the form of the potential has been chosen, the exact parameters are typically determined by empirical fitting: thermodynamic properties such as melting point, heat capacity, etc, are determined from MD simulations, and parameter values are iteratively refined until the simulation output matches experimentally known values [95]. The more stringently the potential is tested, the more valid and informative simulation results it will give.

3. Mechanics of nanocontacts

When the length scale of indentation is reduced toward the atomic scale, the mechanical response of materials differs in several ways. In this section we review phenomena relevant to small-scale indentation mechanics.

At the atomic scale, the indenter's surface is stepped due to its crystalline nature – this leads to a modification of the yield point during indentation, and possibly the mechanisms of dislocation nucleation as well. Adhesion can often be overlooked in experiments carried out in ambient conditions. However, metallic bonding between clean surfaces in UHV and the large surface area to volume ratio of nanoscale contacts makes adhesion (and associated tip wetting) very pronounced. We will also discuss the onset of plasticity in experiments at this length scale, as well as comparisons between one-to-one spatially matched experiments and molecular dynamics simulations.

3.1 Homogeneous and heterogeneous nucleation

We first set the stage with a brief review of dislocation nucleation. In classical dislocation theory, a material yields due to the motion or generation of dislocations [96]. In order to plastically deform a perfect single crystal, it must in effect become imperfect, by dislocation nucleation. (A dislocation is defined as the boundary between slipped and unslipped parts of a crystal.) The shear stress required to induce this co-operative movement of atoms is of the order $\tau_{theo} \approx G/2\pi$, where G is the shear modulus. In macroscopic materials testing, yield usually occurs when the shear stress is only 10^{-4} to 10^{-8} of this theoretical value: The motion of pre-existing dislocations in the material accommodates plastic deformation at comparatively very low loads. Creating new dislocations a large specimen is not usually necessary to plastically deform it. When the length scale of mechanical tests is reduced to the point where the likelihood of finding pre-existing dislocations in the volume under test is very small, yield begins at values much closer to τ_{theo}. This is one of the origins of the well-known indentation size effect in which hardness increases as a function of decreasing indentation depth [97].

During indentation, a force is applied in the direction perpendicular to the surface. The loading of the sample results in a complex sub-surface stress field: It is the magnitude of this stress field, resolved along a slip plane, which determines the load at which the material yields by homogeneous dislocation nucleation.

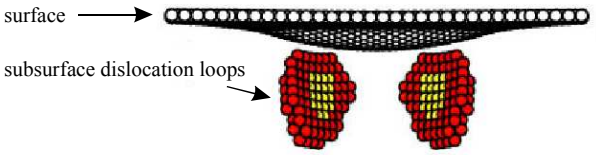

Figure 8: Molecular dynamics simulation of nanoindentation of Au(111) by a spherical indenter, viewed from the side, at the moment of dislocation nucleation. The centrosymmetry parameter, a scalar quantity which reflects the deviations of atoms from symmetric positions, enables the visualization of defect structures (see Ref. [98]). Two partial dislocation loops (red atoms) surround stacking faults (yellow atoms) caused by the slip process. The surface atoms are shown in white, and atoms occupying regular lattice positions are omitted from the illustration. Reprinted figure with permission from Ref. [98]. Copyright 1998 by the American Physical Society.

An atomistic view of dislocation nucleation during indentation first appeared in the landmark molecular dynamics work of Kelchner *et al.* [98]. This study addressed Au(111) under indentation by a smooth sphere. The simulation showed that dislocations were nucleated by slip processes occurring along two of the three {111} planes below the surface, and displaced from the indenter's axis of symmetry. This was an initially surprising result given that the principal shear stress calculated from Hertz theory is expected to be *on* the indenter axis (at a depth of $z = 0.48a$ below the free surface, where a is the indenter radius) [90, 91]. However, when one considers the projection of the shear stress onto the {111} slip planes, one finds that the largest resolved shear stress actually occurs off-axis. The configuration of these dislocation embryos is shown in Figure 8, and is in agreement with simulations on other metals such as Cu(111) and Al(111) [99-101]. The two dislocation loops grow rapidly upon further contact loading and eventually emerge at the surface.

In the above description, dislocation nucleation happens homogeneously: The dislocations are formed within the bulk,

in a region of perfectly crystalline material, when the resolved shear stress reaches a critical value.

The alternative scenario that can transpire is one of heterogeneous nucleation, where the critical stress required to nucleate the dislocation is reduced by some local imperfection. Heterogeneous nucleation can result from (among many things) thermally promoted transient defects [102], point defects [103], indenter surface roughness [102, 104], and surface steps [105, 106].

Using a traditional nanoindenter, the picture of heterogeneous nucleation has been compellingly conveyed by Schuh *et al.*, who noted that the load at which the first pop-in is detected on single crystalline Pt(110) is highly stochastic [103, 107]. By carrying out variable temperature and indentation rate experiments, the authors were able to extract a relatively small activation energy of ~0.28 eV, and an activation volume of ~10Å^3. The minute activation volume, on the order of a point defect, is a clear indication of heterogeneous nucleation: For homogeneous nucleation to occur, a cooperative process of atomic motion taking place in many atomic volumes would be required. The mechanism by which heterogeneous nucleation occurs, however, cannot be derived from indentation response.

3.2 Atomically rough indenters

Looking at indentation near the atomic length scale, one of the leading factors which can contribute to heterogeneous dislocation nucleation is the atomically rough surface of the probe. This roughness is due to the crystalline nature of the indenter, which has been shown to locally enhance contact pressure [108], such that a continuum mechanics description of the contact no longer applies.

The consequences of atomically rough indenters in indentation are best revealed by atomistic simulations where the same experiment can be carried out with both smooth and stepped indenters. Wagner *et al.* modeled indentation response in Al(111) under a smooth repulsive tip and a truncated (111) oriented diamond crystal, both of 50 nm radius, at room temperature and at 0 K [102]. The results show homogeneous nucleation of dislocations in the bulk only at 0 K and with smooth tips, Figure 9 (a). With the presence of thermal energy at 300K, dislocations nucleate at thermally promoted 'hot-spot' transient defects, Figure 9 (b). Introducing indenter roughness leads to the heterogeneous formation of dislocation loops from the surface: At 0 K, the surface loops initiate plastic deformation Figure 9 (d), while at room temperature, it is still favourable to initiate plasticity at thermally promoted defects in the bulk Figure 9 (c). The room temperature surface loops were reversed upon unloading.

One may also expect the indenter radius to modify the importance of stepped indenters: Surface-initiated dislocation loops should propagate into the bulk more readily under the higher stress gradients produced by sharper tips. In recent simulations performed by Shin *et al.* on Cu(111) for atomically rough tips of radii 2.5-20 nm, the expansion of surface-initiated dislocation loops was responsible for plastic deformation at room temperature [104].

On the experimental side, atomic-scale tip characterization is required to study the effect of tip radius and roughness in a systematic way. This constitutes an open area for experiments, suitable for investigation by FIM and SPM (see Section 5).

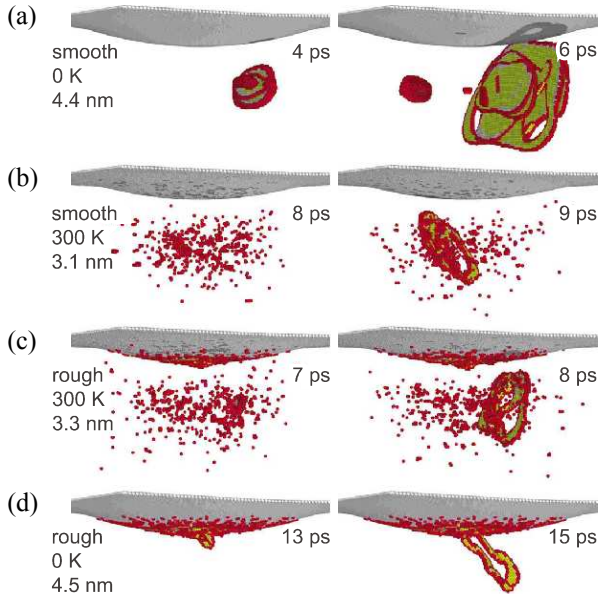

Figure 9: Defect structures in Al(111) under (a,b) smooth and (c,d) atomically rough indenters of radius 50 nm at 0 K and 300 K. Atoms are coloured by the centrosymmetry parameter. Surface atoms appear grey, partial dislocations are shown in red, and stacking faults are yellow. Reprinted with permission from Ref. [102]. Copyright 2008, AIP Publishing LLC.

3.3 Small-scale indentation experiments

Indentation response at length scales comparable to atomistic simulation has been studied by several groups with SPM techniques. In particular, the Rojo group has investigated defect configurations at surfaces using STM. Their experimental work on Au(001) has been supported with molecular dynamics simulations to explain the generation and motion of hillocks seen on the surface at distances of tens of nanometers from indentation sites (shown in Figure 10) [33-37]. The authors found that the shape of the hole left by small indentations, less than 80 nm in width, is determined by the crystal structure's slip plane configuration rather than the shape of the indenter (as per traditional nanoindentation experiments). Also, the terraces created near indentations require substantial mass transport – interestingly, this was found to be mediated by dislocation motion rather than a diffusive mechanism. Monoatomic terraces begin to form at indentation-produced screw dislocations emerging at the surface. As these dislocations move, a monoatomic step is left behind on the crystal surface. Filleter *et al*. have observed the same type of dislocation-mediated mass transport in KBr(100) studied by AFM indentation [26].

On KBr(100), hillocks have also been found around indentation sites. Atomic resolution AFM imaging of the

surface has revealed that the hillocks on KBr correspond to a different defect structure: The two full edge dislocations at each hillock indicate that the defect structure corresponds to a classical indentation rosette [27]. These studies point out the utility of high resolution surface imaging for elucidating sub-surface defect structures and mechanisms of plasticity.

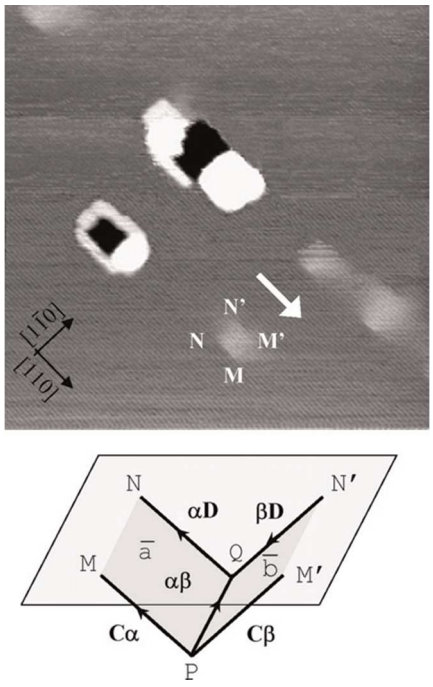

Figure 10: 150nm x 150 nm. The successive emission and glide of dislocation loops from the indentation site results in rows of hillocks seen on the Au(001) surface tens of nm from the center of the indentation. The generation of hillocks has also been observed on Cu(100) [24]. Reprinted with permission from Ref. [37]. Copyright 2008, Taylor & Francis Ltd (http://www.tandfonline.com/).

3.4 Time dependence

Schuh and Lund applied nucleation theory to explain the rate dependence of the first indentation pop-in [**109**], recognizing that the nucleation rate per unit volume of material subjected to shear stress τ can be expressed as

$$\dot{N} = N_0 \, exp\left(-\frac{E_a - \tau v^*}{k_B T}\right), \qquad (1)$$

where N_0 is an attempt frequency prefactor, E_a is the activation energy barrier, v^* is the activation volume, and $k_B T$ is the thermal energy. Under stress-assisted thermal activation, defect nucleation can be triggered with a finite probability at any applied stress, so long as sufficient time is allowed. The nucleation rate framework is also applicable to processes occurring after the first pop-in (albeit with a E_a appropriate to the mechanism, e.g. dislocation glide).

Although single-crystals specimens do not respond viscoelastically (for any reasonable indentation speed) or with continuum creep in atomic-scale nanoindentation, the fact that defect nucleation is thermally activated (Eq. (1)) adds a time dependence to plastic indentation response which resembles a discretized version of creep. In AFM-based atomic-scale indentation of KBr, it was observed that when the maximum indentation load is held constant in time, pop-ins can occur for up to several minutes [110]. The rate of pop-ins is noted to decrease with time which reflects either a work hardening process (increase of E_a for further dislocation nucleation), or the increasing indenter contact area which reduces indentation stress.

This atomic-scale creep behaviour differs from large scale indentation experiments where creep is usually absent before the initial (large) pop-in and is only made possible afterward due to the presence of mobile dislocations [111, 112]. This behaviour is manifest as a continuous sinking of the tip as dislocations glide and multiply. Continuous creep can be caused by other effects such as grain boundary sliding (in polycrystalline samples), dislocation climb, or diffusion (e.g. indium accommodates deformation nearly continuously by low energy self-diffusion [112, 113]).

With sufficient force and displacement resolution, investigations into the discrete nature of creep events are a natural subject for future investigation by atomic-scale nanoindentation.

3.5 Adhesion and tip wetting

Adhesion between indenter and substrate represents another significant departure from large-scale nanoindentation behaviour. Metallic bonding and associated atom transfer from the substrate to the tip, known as tip wetting, were salient features in the early simulation work of Landman *et al*. [78]. No simple analytical model allows the full description of adhesion between different materials – the energy involved in contact separation must overcome the ideal work of adhesion, as well as dissipative processes which make contact separation more energetically costly in practice [114]. For elastic contacts described by the JKR model, one expects that the adhesive force at pulloff increases linearly with surface energy [91]. JKR-type adhesion has been reproduced in atomistic simulations for large scale asperities, as long as the contact separates elastically (lower adhesion energies) [25]. Larger adhesion energies lead to a greater extent of plastic deformation during separation. Contact separation at the atomic scale is typically accompanied by material transfer [115-117]; the hardness of each material and the surface energies involved dictate the directionality and extent of material transfer. For tungsten-gold indentations, we note a wetting behaviour of the tungsten tip surface by gold atoms, with no plastic deformation of the tungsten indenter [118].

There is good experimental evidence that the surface of a clean tungsten indenter undergoes progressive wetting during multiple indentations with gold substrates [119]. In Figure 11 we show the apex of a clean W(111) indenter prepared by FIM and the first 25 load-displacement curves measured while indenting pristine locations of a Au(111) crystal (loading direction only). The first indentation is shown in black, and

subsequent curves are coloured in the indicated sequence. An offset in the rise of repulsive loading is observed for all subsequent curves with respect to the initial indentation which provides a 'left-hand' bound. The depth offset is measured with respect to the detection of a tunneling current (1 GΩ gap resistance) – the observed offsets indicate that a conductive and compressible layer of gold is collected on the tip, up to a thickness of about 0.25 nm (approximately 1-2 layers of gold atoms). (We note that in these experiments, tip wetting is controlled only coarsely by repeated indentation and inferred from force-displacement curves, but it could be deliberately fashioned by thermal evaporation of a known thickness of gold atoms onto the FIM-prepared tip.)

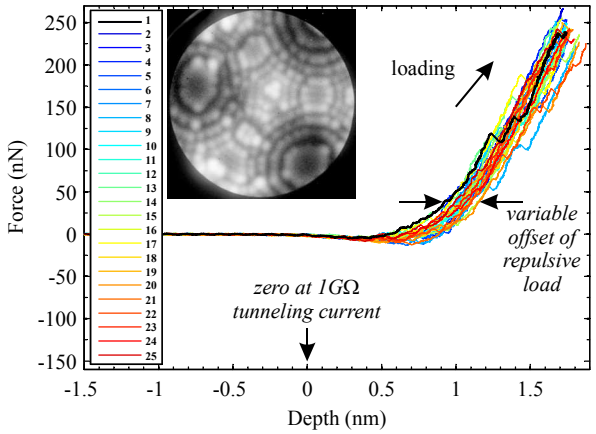

Figure 11: The first 25 indentation curves of a fresh W(111) tip (shown inset) in a Au(111) substrate (loading direction only). From Ref. [119] © IOP Publishing. Reproduced by permission of IOP Publishing. All rights reserved.

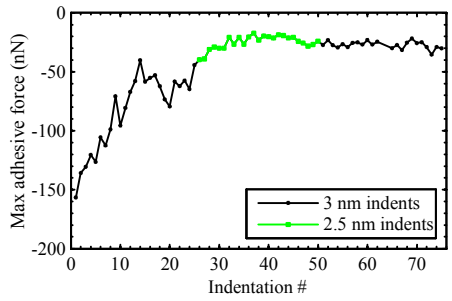

Figure 12: The maximum adhesive force tends toward a constant value after repeated indentation. From Ref. [119] © IOP Publishing. Reproduced by permission of IOP Publishing. All rights reserved.

Another striking experimental observation is a transient behaviour in the maximal pull-off force, with a reduction of about 6× as tip wetting takes place after multiple indentations. Plotted in Figure 12 is the maximum adhesive force (maximally negative) for the initial separations of a tungsten tip from a gold substrate. This behaviour is quantitatively reproducible with freshly prepared tungsten indenters and plateaus with a 1/e decay constant of 11-14 indentation cycles. The reduction in pull-off force may reflect the changing surface energies of the tip-sample system [25], but surface diffusion of Au atoms may also help mediate contact separation at room temperature, similar to the self-healing mechanisms reported for sliding contacts [120]. If the role of surface diffusion is significant, molecular dynamics simulations may not quantitatively reproduce contact separation forces of experiments carried out at room temperature because of the order 10^9 mismatch in time scales [118].

The strong transient behaviour of mechanical properties due to the wetted state of the tip suggests that it is important to characterize and control the indenter surface chemistry (perhaps by saturation of tip wetting) in order to make meaningful comparisons of indentation response at this length scale.

3.6 Capturing the onset of plasticity in experiments

Recent nanoindentation experiments inside a transmission electron microscope have shown that plastic deformation may occur before the first obvious displacement burst is measured in force-displacement curves due to the limited force resolution of traditional nanoindenters [21]. We have studied incipient plasticity with SPM with single nanonewton sensitivity, and have found a clear but stochastic transition from elastic to plastic contact loading on Au(111) [44]. After wetting the tip to saturation to ensure that indentation response reflects the mechanics of the substrate, a 5 × 5 array of indentations was created by approaching the tip toward the sample by 2 nm from the tunneling setpoint. Figure 13 shows a topographic STM image of the Au(111) surface before (a) and after (b) indentation. The indentation depth was chosen to be near the onset of plastic deformation; in this array of indentations, some sites show permanent impressions (bold numbers), while at others, no residual impression is imaged.

The elastic/plastic nature of the indentation sites determined by residual impression imaging has a direct correspondence with features of the load-displacement curves. The elastic sites show very well overlapping loading and unloading curves at repulsive loads, whereas the curves become separated when plasticity is initiated. In fact, the separation between these curves at low repulsive loads (at about 10 nN, known as the 'sink-in' depth) is the best quantitative indicator of plasticity that can be derived from the force-displacement data.

It is important to note that the tip wetting layer complicates the measurement of mechanical properties: At a depth less than ~0.8 nm, the two elastic indentations shown in Figure 13(c) and (d) differ substantially due to the stochastic rearrangement of the tip wetting layer. Although no plasticity is nucleated in the Au(111) crystal in either indentation, they are associated with very different hysteresis energies of 47 and 83 eV respectively.

Comparing the average hysteresis energies of elastic and plastic curves, we conclude that about 70 eV is available for the creation of plastic damage in the sample. This energy corresponds to that of an edge dislocation threading ~12 atomic planes [96], or the energy required to break several tens of atomic bonds [121]. The small energy budget is commensurate

with the lack of hillocks (see Section 3.3) imaged on the surface in the vicinity of the indentations; we hypothesize that the final defect configuration consists solely of a vacancy cluster (hole), with no remnant dislocations or other extended defects.

In this study, we have quantified the scale of the smallest permanent impression producible by indentation. The experiment is very well defined with its FIM-characterized 9.5 nm radius W(111) tip and opens up several interesting questions which might be addressed from the modelling side: Can the observed energy budget be reproduced? What is the origin of the minimum plastic energy? What atomistic processes governs the initiation of plastic deformation?

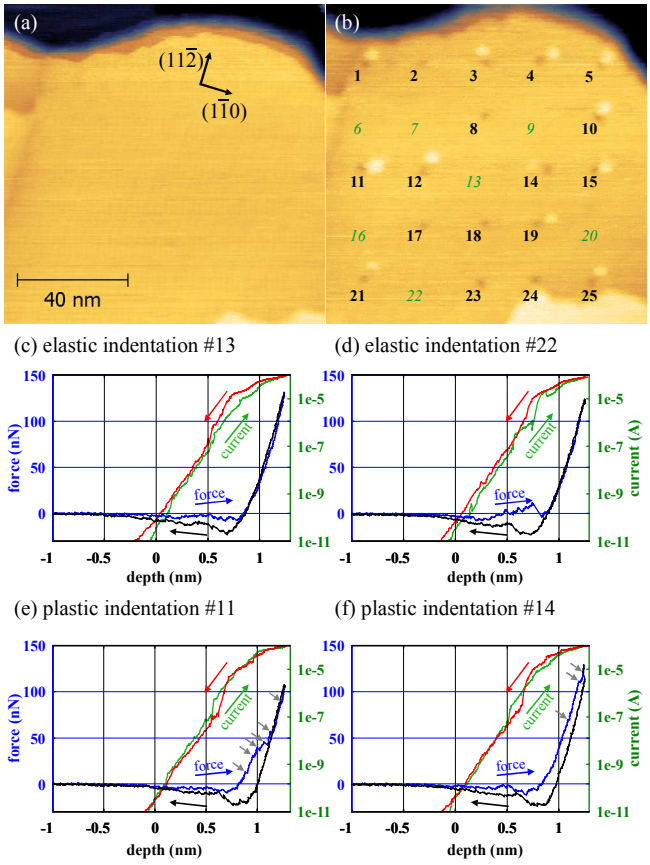

Figure 13: (a) Au(111) terrace before and (b) after a 5 × 5 indentation array with 20 nm spacing between indents (20 pA, -0.05 V sample bias). Indentations were carried out in the numbered sequence. Bolded numbers indicate plastic sites; italicized numbers indicate elastic sites. Force and current (-0.05V sample bias) recorded during indentation at elastic sites, (c) and (d), and plastic sites, (e) and (f). Loading and unloading directions are indicated by arrows. Additional arrows in (e) and (f) point to pop-in discontinuities in the force channel. Reprinted figure with permission from Ref. [44]. Copyright 2013 by the American Physical Society.

3.7 One-to-one spatial matching of experiments and simulation

So far, rather few indentation experiments have permitted direct comparison with molecular dynamics simulations at the same length scale: The hillocks created during STM indentation (Figure 10) have been reproduced in simulations [34], and the mechanisms of dislocation nucleation on stepped gold surfaces during AFM indentation have been modeled [105]. Direct comparison between experiments and atomistic simulation has enjoyed more popularity in the field of atomic scale friction [120, 122-124], where friction fore microscopy has become a popular tool for studying sliding single-asperity contacts on the atomic scale [125, 126].

We have recently compared SPM-based nanoindentation of Au(111) with atomistic simulations using both an "atomic tip" (built from a W(111) single crystal) and a "smooth tip" (a repulsive potential), both with 4.1 nm radii [118]. The smooth tip favours homogeneous dislocation nucleation in the bulk, whereas defects are nucleated heterogeneously at the tip-substrate interface with atomic tips. This supports our hypothesis in previous experiments, where the highly stochastic distribution of the load at the first pop-in was interpreted as an indicator of heterogeneous nucleation [44].

Numerous experimental observations are supported by the simulations, including adhesion and tip wetting, material pile-up, and a hexagonal indent morphology (Figure 14). Some behaviours, however, are not well-reproduced: Notably, the maximum of the adhesive pull-off force is significantly higher in simulation than in experiment. This points to the need to close not only the length scale, but the time scale gap, by taking advantage of advanced theoretical techniques to extend accessible time scales from picoseconds to milliseconds or seconds [127, 128].

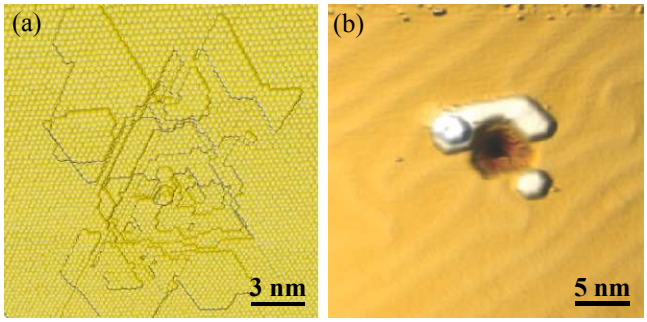

Figure 14: (a) Surface morphology of Au(111) after indentation by a W(111) atomic tip in a molecular dynamics simulation. (b) 3D rendering of the surface topography of Au(111), measured by STM, after an indentation experiment (9 pA, -0.9 V). The herringbone reconstruction of the gold surface has rearranged in the vicinity of the indentation to accommodate changes in surface stress. From Ref. [118] © IOP Publishing. Reproduced by permission of IOP Publishing. All rights reserved.

4. Electronic transport through nanocontacts

Electron transport happens quite differently through nanoscale metallic contacts compared to macroscopic conductors. The conductance of a macroscopic wire is proportional to its cross-sectional area, A, and inversely proportional to its length, L, that is, $G = \sigma A/L$ where σ is the conductivity of the material. In nanoscale contacts, the distance an electron travels between scattering events is usually much larger than the dimensions of the system. As a result, the nature of conductance is very different: Increasing the length of a

nanoscale constriction, for example, doesn't affect its resistance.

In slightly more formal terms, when the dimensions of a wire or constriction are reduced such that they are much smaller than the elastic mean free path of electrons, the electrons will undergo ballistic transport. Using a semiclassical approach, Sharvin obtained the conductance for a pure ballistic contact as [129]

$$G = \frac{2e^2}{h}\left(\frac{k_F a}{2}\right)^2, \qquad (2)$$

where e is the electron charge, h is Planck's constant, k_F is the Fermi wavevector, and a is the contact radius. In a fully quantum mechanical approach, the conductance of a constriction is described by the Landauer-Büttiker formalism [130, 131]: The lateral confinement of electrons gives rise to quantized eigenchannels in the constriction, each contributing (under maximum transmission probability) a conductance of $G_0 = 2e^2/h$ (the quantum of conductance). Conductance quantization was first demonstrated experimentally in 1988 for a GaAs-AlGaAs heterostructure system where the width of a constriction in a two-dimensional electron gas could be continuously varied by an applied gate voltage [132, 133].

Roughly speaking, for a metallic constriction with a cross-section of a small number of atoms, i.e close to the Fermi wavelength, each atom in the constriction will contribute about one conductance quantum. As the number of atoms in the constriction grows, fully open (transmission probability = 1) channels are added. For larger contacts, beyond ~6 atoms, several partially open channels can be active simultaneously which blurs the quantization to some extent [134].

Atomic-sized constrictions have been studied extensively using mechanically controlled break junctions [135-139], STM [140-145], and *in situ* TEM experiments [146-148]. If one constructs a histogram from the obtained conductance values for many contact making/breaking cycles, peaks appear at integer values of G_0, indicating conductance quantization. In these atomic-scale contacts, abrupt changes between stable atomic configurations can lead to jumps of order G_0 in the measured conductance. The addition of discrete mechanical rearrangements to the already quantized conductance complicates the interpretation of experimental results and has been the subject of debate. The emergent picture is one in which conductance quantization explains the statistical peaks in histograms, and atomic rearrangements are responsible for jumps between different values in individual traces [149].

Atomic-scale constrictions provide a starting point for understanding some of the features of the conductance observed during atomic-scale indentation. However, break-junction contacts are rather different from the contact configuration in an indentation experiment: Firstly, the indenter and surface are usually made up of different materials because of the demands of mechanical properties testing (the indenter should be hard compared to the sample). Secondly, during indentation, extreme stresses are applied in the sample. The measured conductance under maximal indentation load is a probe of transport through the compressed volume including any defect structures which might reside within it.

In the following sections, we discuss recent experimental results on the conductance of atomic-scale indentation contacts and first principles calculations of electronic transport through model systems for interfaces and defect structures.

4.1 Interface and defect scattering

An indentation-formed nanocontact between a tungsten tip and gold surface provides a means to study electronic transport between metals of different electronic structure. The well-defined indenter size obtained from FIM, combined with force-depth determination, gives a good experimental handle on the cross-sectional area during contact formation. Estimating the contact area by several methods for elastic and plastic contacts, we have found that the junction conductance falls much below the expected order 1 G_0 per atom Sharvin conductance ($g_{Sharvin} = 13.8\ G_0/\mathrm{nm}^2$ for this system) [150]. In first principles density functional theory calculations, the electronic conductance for both Au(111) and W(111), when considered separately, is high and close to the Sharvin value. When conductance is calculated across a Au(111)/W(111) lattice-matched interface, a large fraction of the electrons are backscattered leading to a much lower conductance of only $g_{W/Au} = 2.8\ G_0/\mathrm{nm}^2$, illustrated in Figure 15. The large decrease of conductance is due to the mismatched s wave-like electron modes in gold and the d wave-like modes in tungsten.

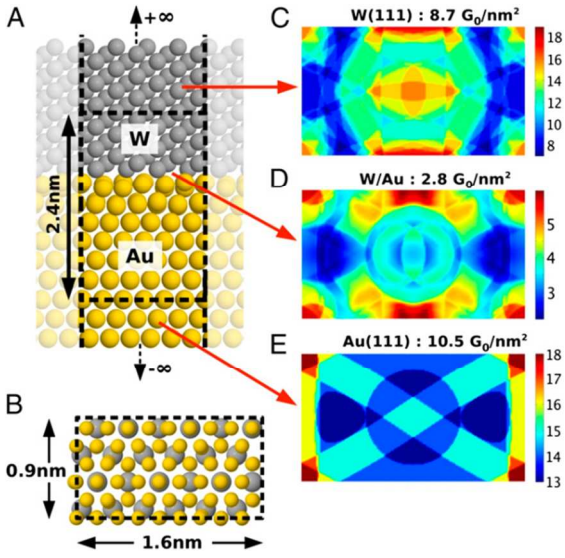

Figure 15: (A) Side view and (B) cross-section of the atomic structure of the W(111)-Au(111) interface. The dashed black lines and associated dimensions delimit the simulation box for the *ab initio* transport calculations. (C-E) present the transmission coefficient in reciprocal space for pure W(111), the W(111)-Au(111) interface, and pure Au(111), respectively. The total conductance per unit area is also shown. Note the much reduced colour scale-bar in (D) for the W(111)-Au(111) interface. From Ref. [150].

The calculated $g_{W/Au}$ quantitatively reproduces the upper limit of conductance measured during indentation experiments. However, $g_{W/Au}$ is only an upper bound since defects within the gold generated by plastic deformation serve to further reduce the measured conductance. First principles calculation of electron transport through entire dislocation structures is beyond current computational capabilities. In attempt to model the effect of imperfections and defects on electron transport during indentation, random atomic deviations from ideal lattice sites (disorder) and random vacancies have been considered in gold crystals.

When disorder is added to the crystal, atoms become simultaneously closer and farther apart. The increased distance between gold atoms reduces electronic hopping and contributes additional resistance. The conductance is found to decrease approximately linearly with the intensity of disorder (defined as a percentage of the relaxed nearest neighbour distance), reaching a factor of two drop at 25% disorder. A reasonable estimate for the disorder parameter from molecular dynamics simulations is in the vicinity of 10% which suggests a 0.75 transmission probability modification due to disorder.

Vacancies in gold induce local perturbations in potential and act as scattering sites for electron waves. Conduction decreases due to backscattering, and ballistic transport is nearly quenched by a 10% vacancy density. The resulting electronic conductance is reduced by a factor of two at this vacancy density.

With the combined effects of interface resistance, disorder, and vacancy scattering, the modified conductance density is expected to be about 1 G_0/nm^2. This represents a reduction by over an order of magnitude from the Sharvin condition of 13.8 G_0/nm^2. In experiments, the measured conductance densities fall within a range between 0.02-4.9 G_0/nm^2. This large range reflects the highly stochastic nature of defect structures which can occur during indentation, as well as other sources of variability (e.g. tip wetting discussed in Section 4.2).

Direct measurements of conductance across bimetallic interfaces or individual grain boundaries are exceedingly rare, due to the difficulties in creating a well-defined contact area at small dimensions and characterizing the orientation of the interface components. Scanning tunneling potentiometry [151] can be used to map the drop in chemical potential across grain boundaries in thin films of gold, yielding reflection coefficients between 0.7 and 0.9 [152]. The lack of characterization of interface structure, however, inhibits direct comparison with atomistic models. Recently, the direct measurement of resistance jumps across copper nanowire grain boundaries was obtained by STM with a four-point probe [153]. In this work, electron backscatter diffraction images were used to identify the types of grain boundaries in the wires which were contacted by multiple STM tips. This study was accompanied by first principles calculations showing that varying the of structural symmetry of a grain boundary can cause order-of-magnitude variations in electronic conductance. Conduction across coincidence boundaries (e.g. twin) occurs more easily than random grain boundaries. A similar four-point probe STM technique has also been applied to boundaries in graphene sheets [154].

Theoretical investigation of electron transport across boundaries is not hampered by issues of sample preparation and contact formation which are present in experiments, and the study of electronic transport across various orientations of grain and twin boundaries [155, 156], stacking faults [157], and intermetallic interfaces [158] has been actively pursued. The presence of vacancies, the orientation of grain boundaries, and disorder contribute significantly to reflectivity at interfaces. These results imply that the control over grain boundary geometry in device interconnects is crucial for building low-resistance connections. For indentation testing, the results suggest that nanoscale contact area cannot be naïvely estimated from a Sharvin estimation – the effects of interfaces, disorder, and vacancies can dominate the measured transport behaviour.

4.2 Tip wetting and conductance

In section 3.5, we reported on the transient decay of the adhesion force after repeatedly indenting a W(111) tip in a Au(111) surface. The transient behaviour occurs as the tungsten tip collects gold atoms from the surface after many indentation cycles. In these indentation experiments, the maximal conductance of the junction decreases dramatically by a factor of ~12× from its initial value [119]. This happens at the same 1/e decay rate as the adhesive force (11-14 indentation cycles in this experiment).

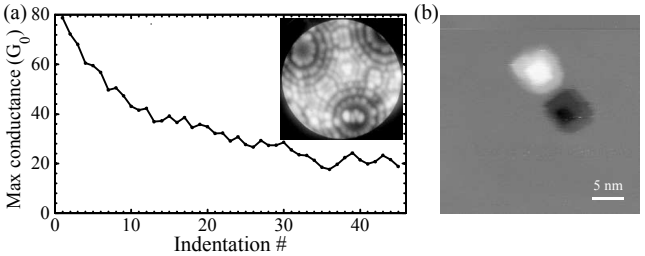

Figure 16: (a) Maximum conductance during a sequence of 1.5 nm deep indentations on Cu(100). Indentations were carried out with STM only, i.e. without force or true depth sensing. Inset: FIM image of the 7.2 nm radius W(111) indenter. (b) STM image of the typical square shaped hole and pile-up reflecting the symmetry of the substrate (9 pA, -0.8V). From Ref. [119]

The transient decay of maximal conductance also occurs in the STM indentation of a W(111) tip into a Cu(100) single crystal, shown in Figure 16 for an indentation depth of 1.5 nm. Here, the maximum conductance decreases from an initial value of ~80 G_0 to a plateau at ~20 G_0. Since a dozen STM images and two smaller indentations were performed before the start of this sequence, we expect that the magnitude of the conductance drop would be greater than 4× for a pristine tungsten tip. The presence of this effect in two different metallic substrates gives us a good indication of its universality.

As the tip becomes wetted with gold (or copper), we expect conductance drops due to the build-up of additional interface

layers which will scatter electron waves. The mismatch between the tip's bcc tungsten lattice and the sample's fcc gold lattice should also create a region of geometric frustration at the boundary between the two crystals: there is no way to arrange the atoms of these two materials to form a matched crystalline interface. Electronic effects due to strained lattices may also be important [159].

The understanding of atomistic structures at the interface and their evolution as a function of tip wetting is an important future direction for modelling: How are transferred substrate atoms bonded to the tip? Are they lattice matched to the tip's crystalline structure? If so, how do they transition to the substrate lattice when an indentation contact is formed? How is the geometric frustration handled at the apex? What do the atomic structures mean for electronic transport properties? On the experimental side, these results contribute to the growing evidence that the surface composition of indenters substantially affects both mechanical and electrical indentation response.

5. Future directions

In this article, we have presented some open questions arising from recent experimental work. There is a particular need for elucidating atomistic processes and configurations during indentation in order to understand the origins of the minimum plastic energy [44], defect configurations within the substrate [44, 119], and the electronic conductance of complex interfaces [119, 150].

Because the quantities measured during experiments (force, displacement, and derived quantities) do not directly give access to the mechanisms of plasticity at the atomic level, one must turn to the quantitative comparisons with simulations. By increasing the level of experimental fidelity at the atomic scale, we hope to make this comparison as direct as possible. New avenues for investigation are suggested here in order to motivate connections between experiments and simulations.

5.1 Indenter geometry

The ability to readily switch between indenters in simulations (smooth repulsive potentials, atomically rough indenters with different crystal orientations) has led to the discovery of several different modes of dislocation nucleation and accommodation of plastic deformation. We imagine that an interchange between atomic-scale indenter geometries in experiments could also benefit our understanding of nanoscale plasticity.

Preparation of indenters by FIM gives the experimentalist an exquisite characterization of the tip structure and control over the surface chemistry. There is also an opportunity to control tip radii by field evaporation [66] or by other *in situ* etching procedures (e.g. with nitrogen [160-162] or oxygen gases [163, 164]). The crystallographic orientation of the wire used to fabricate the tip is a straightforward parameter to use to control the atomic-scale surface step height and geometry at the apex (step height 's' in Figure 7). Together, the combination of tip radii and step configurations may be able to clarify the competition between surface-initiated and bulk-initiated plastic mechanisms [102, 104].

There is also an opportunity to borrow from other active areas of research in the FIM community to create non-spherical indenters at the atomic scale. Pyramidal tip geometries are the basis of many ultra-sharp tips used for coherent electron and ion beam sources [165, 166]. A pyramidal geometry is also desirable for mechanical testing because of its simplified contact-area function [4]. These structures are formed at the end of tips by faceting: First, the relative surface energies of the tip's atomic planes is altered either by deposition of ad-layers of noble metals on W tips [165, 167-169], oxygen on Ir tips [170], or applying large electric fields [171-174]. Then, upon annealing under these modified conditions, the favoured planes expand and intersect to form an atomic-scale pyramid.

5.2 The 'pop-out'

We introduced the 'pop-out' in Figure 4 as a feature of atomic-scale nanoindentation which is associated with the partial reversal of plasticity during unloading. While it is not seen in shallow indentations on pristine Au(111) surfaces [44], it does appear in deeper indentations (such as the one reported in Figure 4) and in other studies where surface characterization is lacking [23]. The origins of the 'pop-out' remain largely unexplored and deserve more attention. Processes which reverse plastic deformation are inherently interesting: What types of damage can be reversed? Can one design materials with enhanced self-healing properties?

5.3 Work hardening and defect configuration

The cyclic loading of materials can affect mechanical properties by inducing work hardening when the density of dislocations becomes sufficient that they begin to interact, pin, and hamper further deformation. At the atomic scale, cyclic loading has been observed to produce a hardening shakedown behaviour [23], but the absence of surface imaging makes these results difficult to interpret.

At very low loads – at the threshold of plastic deformation – there is evidence that only a vacancy cluster (hole of missing atoms) is produced in the substrate (by energetic evidence and high resolution STM surface imaging [44, 119], Section 3.5). The extremes of vacancy cluster formation on the one hand and work hardening on the other suggest that there should be a critical point at which dislocations become permanent in the material (room temperature irreversible), and the repeated indentation of such a dislocation-filled sample should reveal dramatically altered mechanical properties.

5.4 Chemical composition

Given the relative importance of surfaces at nanoscale dimensions, the chemical composition of indenters becomes a key variable which must be controlled, or at least characterized, in experiments. Chemical composition directly determines surface energies, which control adhesion and atom transfer [25]. Experimentally, we know that clean tungsten tips and gold-wetted tungsten tips show very different adhesive and

electrical properties [119]. In addition to the field evaporation method used to expose clean indenter surfaces, the noble-metal plated tips proposed in Section 5.1 may be a reasonable method to vary surface chemical composition. Passivation by reaction of tungsten tips with N or O atoms (from N_2 or O_2 gases [175]) may be of interest to control adhesive forces or alter surface step structures while maintaining the overall indenter radius.

5.5 Electronic Transport

As we discussed in Section 4.1, the electronic transparency of interfaces, grain boundaries, and disorder structures are active topics of theoretical research. The FIM/SPM indentation technique can contribute experimental data to this area, since junctions with a well-defined contact area can be created between pairs of metals with arbitrary crystallographic orientation.

5.6 Interplay of electronic and mechanical properties

Mechanical rearrangements in atomic-scale tensile contacts (e.g. break junction, AFM tip retraction) result in abrupt and simultaneous changes in the measured force and current, usually straightforwardly connected to the evolving contact area [135, 176, 177]. During indentation, mechanical pop-ins are often correlated with discrete jumps in indentation conductance, but the relationship is not clear-cut [45]. The sign of the correlation between force and current jumps is not constant – an indentation pop-in can cause either an increase or a decrease in electronic conductance (speculatively due to a simultaneously changing contact area and sub-surface defect structure).

A better understanding of the relationship of electronic and mechanical properties during indentation may also uncover interesting interplay: Can mechanical rearrangements modify the junction conductance, leading to localized heating from inelastic scattering which in turn activates more mechanical changes? This would provide atomic-scale insight into processes such as cold welding.

5.7 Time scales in experiments and modelling.

Through the refinement and combination of FIM and SPM techniques (Section 2), the length scale of indentation experiments has been shrunk to atomic dimensions where direct comparison can be carried out with atomistic simulations. There remains, however, a $10^9\times$ mismatch in time scales between the two. Evidence that diffusive mechanisms may mediate contact adhesion [119], as they can in friction [120], is a strong reason to try to close this time gap.

From the computational side, emerging methods that allow diffusion to be taken into account should help in this effort [127, 128]. In experiments, the most practical way to test for diffusive mechanisms is to attempt to freeze them out in variable (or low) temperature experiments.

6. Conclusion

The length scale gap between molecular dynamics simulations and nanoindentation experiments can be closed with a SPM-based approach to depth-sensing indentation, employing FIM to characterize the atomic structure of indenters and to guarantee their clean surface composition. The number of well-defined experiments at this length scale is still limited, but the potential for the investigation of new materials and tip geometries, as well as the collaboration with modelling, is very promising. Future work on time-scale matching, both through variable temperature experiments and emerging computational methods will help to fill out the picture of how thermal activation and processes such as diffusion affect the way materials yield. Indentation contacts also provide a test-bed for well-defined contacts between electronically dissimilar metals, as an aid to the design of the next generation of nanoelectronic devices.

Acknowledgments

Funding from NSERC, CIFAR, and RQMP is gratefully acknowledged.

Notes and references

[a] Department of Physics, Faculty of Science, McGill University, Montréal, Québec, H3A 2T8, Canada.
[a] current address: IBM Research Division, Almaden Research Center, 650 Harry Road, San Jose, CA, USA.

1. C. Lu, Y.-W. Mai, and Y.-G. Shen. Recent advances on understanding the origin of superhardness in nanocomposite coatings: A critical review. *Journal of Materials Science*, 41 (3): 937–950, 2006. doi: 10.1007/s10853-006-6577-9.
2. K. Kumar, H. Van Swygenhoven, and S. Suresh. Mechanical behavior of nanocrystalline metals and alloys. *Acta Materialia*, 51 (19): 5743–5774, 2003. doi: 10.1016/j.actamat.2003.08.032.
3. J. Cuy, A. Mann, K. Livi, M. Teaford, and T. Weihs. Nanoindentation mapping of the mechanical properties of human molar tooth enamel. *Archives of Oral Biology*, 47 (4): 281–291, 2002. doi: 10.1016/S0003-9969(02)00006-7.
4. A. C. Fischer-Cripps. *Nanoindentation*, volume 1 of *Mechanical Engineering Series*. Springer, New York, 2011. ISBN 978-1-4419-9871-2. doi: 10.1007/978-1-4419-9872-9. URL http://-www.springerlink.com/index/10.1007/978-1-4419-9872-9.
5. B. R. Lawn and R. F. Cook. Probing material properties with sharp indenters: a retrospective. *Journal of Materials Science*, 47 (1): 1–22, 2012. doi: 10.1007/s10853-011-5865-1.
6. C. A. Schuh. Nanoindentation studies of materials. *Materials Today*, 9 (5): 32–40, 2006.
7. A. Gouldstone, N. Chollacoop, M. Dao, J. Li, A. M. Minor, and Y.-L. Shen. Indentation across size scales and disciplines: Recent developments in experimentation and modeling. *Acta Materialia*, 55 (12): 4015–4039, 2007. doi: 10.1016/j.actamat.2006.08.044.
8. S. B. Sinnott, S.-j. Heo, D. W. Brenner, J. A. Harrison, and D. L. Irving. Computer Simulations of Nanometer-Scale Indentation and Friction. In B. Bhushan, editor, *Nanotribology and Nanomechanics I*, chapter 10. Springer Berlin Heidelberg, Berlin, Heidelberg, 2011. ISBN 978-3-642-15282-5. doi: 10.1007/978-3-642-15283-2. URL http://link.springer.com/10.1007/978-3-642-15283-2.
9. M. Greenwald. Beyond benchmarking - how experiments and simulations can work together in plasma physics. *Computer Physics Communications*, 164 (1-3): 1–8, 2004. doi: 10.1016/j.cpc.2004.06.001.

10. A. Martini. Progress in Tribology Through Integrated Simulations and Experiments. *Tribology Letters*, 50 (1): 1–1, 2013. doi: 10.1007/s11249-013-0125-y.
11. H. Hertz. *Miscellaneous papers*. Macmillan, London, 1896.
12. M. Doerner and W. Nix. A method for interpreting the data from depth-sensing indentation instruments. *Journal of Materials Research*, 1 (04): 601–609, 1986. doi: 10.1557/JMR.1986.0601.
13. W. C. Oliver and G. M. Pharr. An improved technique for determining hardness and elastic modulus using load and displacement sensing indentation experiments. *Journal of Materials Research*, 7 (06): 1564–1583, 1992. doi: 10.1557/JMR.1992.1564.
14. W. Oliver and G. Pharr. Measurement of hardness and elastic modulus by instrumented indentation: Advances in understanding and refinements to methodology. *Journal of Materials Research*, 19 (1): 3–20, 2004. doi: 10.1557/jmr.2004.19.1.3.
15. B. Bhushan, A. V. Kulkarni, W. Bonin, and J. T. Wyrobek. Nanoindentation and picoindentation measurements using a capacitive transducer system in atomic force microscopy. *Philosophical Magazine A*, 74 (5): 1117–1128, 1996. doi: 10.1080/01418619608239712.
16. S. A. Syed Asif, K. J. Wahl, and R. J. Colton. Nanoindentation and contact stiffness measurement using force modulation with a capacitive load-displacement transducer. *Review of Scientific Instruments*, 70 (5): 2408, 1999. doi: 10.1063/1.1149769.
17. S. A. Syed Asif, R. J. Colton, and K. J. Wahl. Nanoscale Surface Mechanical Property Measurements: Force Modulation Techniques Applied to Nanoindentation. In *Interfacial Properties on the Submicrometer Scale*, chapter 13. ACS Books, Washington, DC, 2001. doi: 10.1021/bk-2001-0781.ch013.
18. G. M. Odegard, T. S. Gates, and H. M. Herring. Characterization of viscoelastic properties of polymeric materials through nanoindentation. *Experimental Mechanics*, 45 (2): 130–136, 2005. doi: 10.1007/BF02428185.
19. G. Lewis and J. S. Nyman. The use of nanoindentation for characterizing the properties of mineralized hard tissues: state-of-the art review. *Journal of biomedical materials research. Part B, Applied biomaterials*, 87 (1): 286–301, 2008. doi: 10.1002/jbm.b.31092.
20. O. Franke, M. Göken, M. Meyers, K. Durst, and A. Hodge. Dynamic nanoindentation of articular porcine cartilage. *Materials Science and Engineering: C*, 31 (4): 789–795, 2011. doi: 10.1016/j.msec.2010.12.005.
21. A. M. Minor, S. A. S. Asif, Z. Shan, E. A. Stach, E. Cyrankowski, T. J. Wyrobek, and O. L. Warren. A new view of the onset of plasticity during the nanoindentation of aluminium. *Nature materials*, 5 (9): 697–702, 2006. doi: 10.1038/nmat1714.
22. B. Bhushan and V. N. Koinkar. Nanoindentation hardness measurements using atomic force microscopy. *Applied Physics Letters*, 64 (13): 1653, 1994. doi: 10.1063/1.111949.
23. G. L. W. Cross, A. Schirmeisen, P. H. Grütter, and U. Dürig. Plasticity, healing and shakedown in sharp-asperity nanoindentation. *Nature materials*, 5 (5): 370–6, 2006. doi: 10.1038/nmat1632.
24. T. Filleter and R. Bennewitz. Nanometre-scale plasticity of Cu(100). *Nanotechnology*, 18 (4): 044004, 2007. doi: 10.1088/0957-4484/18/4/044004.
25. J. Song and D. Srolovitz. Adhesion effects in material transfer in mechanical contacts. *Acta Materialia*, 54 (19): 5305–5312, 2006. doi: 10.1016/j.actamat.2006.07.011.
26. T. Filleter, S. Maier, and R. Bennewitz. Atomic-scale yield and dislocation nucleation in KBr. *Physical Review B*, 73 (15): 155433, 2006. doi: 10.1103/PhysRevB.73.155433.
27. P. Egberts, T. Filleter, and R. Bennewitz. A kelvin probe force microscopy of charged indentation-induced dislocation structures in KBr. *Nanotechnology*, 20 (26): 264005, 2009. doi: 10.1088/0957-4484/20/26/264005.
28. G. Binnig and H. Rohrer. Scanning tunneling microscopy - from birth to adolescence. *Reviews of Modern Physics*, 59 (3): 615–625, 1987. doi: 10.1103/RevModPhys.59.615.
29. C. J. Chen. *Introduction to Scanning Tunneling Microscopy*. Oxford University Press, Oxford, 2nd edition, 2008.
30. J. A. Stroscio and W. J. Kaiser, editors. *Scanning Tunneling Microscopy*. Academic Press, San Diego, 1st edition, 1993.
31. D. Sarid. *Scanning Force Microscopy*. Oxford University Press, New York, 1994.
32. F. J. Giessibl. Advances in atomic force microscopy. *Reviews of Modern Physics*, 75 (3): 949–983, 2003. doi: 10.1103/RevModPhys.75.949.
33. J. de la Figuera, M. González, R. Garcá-Martnez, J. Rojo, O. Hernán, A. Vázquez de Parga, and R. Miranda. STM characterization of extended dislocation configurations in Au(001). *Physical Review B*, 58 (3): 1169–1172, 1998. doi: 10.1103/PhysRevB.58.1169.
34. O. Rodrguez De La Fuente, J. A. Zimmerman, M. A. González, J. de La Figuera, J. C. Hamilton, J. M. Rojo, and W. W. Pai. Dislocation Emission around Nanoindentations on a (001) fcc Metal Surface Studied by Scanning Tunneling Microscopy and Atomistic Simulations. *Physical Review Letters*, 88 (3): 1–4, 2002. doi: 10.1103/PhysRevLett.88.036101.
35. E. Carrasco, O. Rodrguez De La Fuente, M. A. González, and J. M. Rojo. Dislocation cross slip and formation of terraces around nanoindentations in Au(001). *Physical Review B*, 68 (18): 1–4, 2003. doi: 10.1103/PhysRevB.68.180102.
36. E. Carrasco, M. González, O. Rodrguez de la Fuente, and J. M. Rojo. Ánalysis at atomic level of dislocation emission and motion around nanoindentations in gold. *Surface Science*, 572 (2-3): 467–475, 2004. doi: 10.1016/j.susc.2004.09.017.
37. E. Carrasco, O. Rodrguez De La Fuente, and J. M. Rojo. Dislocation emission at the onset of plasticity during nanoindentation in gold. *Philosophical Magazine*, 88 (3): 281–296, 2008. doi: 10.1080/14786430701798951.
38. P. Tangyunyong, R. Thomas, J. Houston, T. Michalske, R. Crooks, and A. Howard. Nanometer-scale mechanics of gold films. *Physical Review Letters*, 71 (20): 3319–3322, 1993. doi: 10.1103/PhysRevLett.71.3319.
39. C. Lee, X. Wei, J. W. Kysar, and J. Hone. Measurement of the elastic properties and intrinsic strength of monolayer graphene. *Science*, 321 (5887): 385–8, 2008. doi: 10.1126/science.1157996.
40. S. O. R. Moheimani. Invited review article: accurate and fast nanopositioning with piezoelectric tube scanners: emerging trends and future challenges. *Review of Scientific Instruments*, 79 (7): 071101, 2008. doi: 10.1063/1.2957649.
41. P. Egberts and R. Bennewitz. Atomic-scale nanoindentation: detection and identification of single glide events in three dimensions by force microscopy. *Nanotechnology*, 22 (42): 425703, 2011. doi: 10.1088/0957-4484/22/42/425703.
42. S. A. Joyce and J. E. Houston. A new force sensor incorporating force-feedback control for interfacial force microscopy. *Review of Scientific Instruments*, 62 (3): 710, 1991. doi: 10.1063/1.1142072.
43. U. Dürig, L. Novotny, B. Michel, and A. Stalder. Logarithmic current-to-voltage converter for local probe microscopy. *Review of Scientific Instruments*, 68 (10): 3814, 1997. doi: 10.1063/1.1148005.
44. W. Paul, D. Oliver, Y. Miyahara, and P. H. Grütter. Minimum Threshold for Incipient Plasticity in the Atomic-Scale Nanoindentation of Au(111). *Physical Review Letters*, 110 (13): 135506, 2013. doi: 10.1103/PhysRevLett.110.135506.
45. W. Paul. *Atomically defined tips in scanning probe microscopy*. PhD thesis, McGill, 2013.
46. M. El Ouali. *Nanometre scale indentation: effect of very sharp indenters on adhesion, plasticity, and electronic transport*. PhD thesis, McGill University, 2010.
47. C. Wöll, S. Chiang, R. Wilson, and P. Lippel. Determination of atom positions at stacking-fault dislocations on Au(111) by scanning tunneling microscopy. *Physical Review B*, 39 (11): 7988–7991, 1989. doi: 10.1103/PhysRevB.39.7988.
48. J. V. Barth, H. Brune, G. Ertl, and R. Behm. Scanning tunneling microscopy observations on the reconstructed Au(111) surface: Atomic structure, long-range superstructure, rotational domains, and surface defects. *Physical Review B*, 42 (15): 9307–9318, 1990. doi: 10.1103/PhysRevB.42.9307.
49. C. Schönenberger and S. Alvarado. A differential interferometer for force microscopy. *Review of Scientific Instruments*, 60: 3131, 1989.
50. D. Tabor. *The Hardness of Metals*. Clarendon Press, Oxford, 1951.
51. R. Ragan, D. Ohlberg, J. J. Blackstock, S. Kim, and R. S. Williams. Atomic Surface Structure of UHV-Prepared Template-Stripped Platinum and Single-Crystal Platinum (111). *Society*, (111): 20187–20192, 2004.

52. E. I. Altman and R. J. Colton. The interaction of C60 with noble metal surfaces. *Surface Science*, 295 (1-2): 13–33, 1993. doi: 10.1016/0039-6028(93)90181-I.
53. M. Higo, K. Fujita, Y. Tanaka, M. Mitsushio, and T. Yoshidome. Surface morphology of metal films deposited on mica at various temperatures observed by atomic force microscopy. *Applied Surface Science*, 252 (14): 5083–5099, 2006. doi: 10.1016/j.apsusc.2005.07.034.
54. M. Okano, K. Kajimura, S. Wakiyama, F. Sakai, W. Mizutani, and M. Ono. Vibration isolation for scanning tunneling microscopy. *Journal of Vacuum Science & Technology A: Vacuum, Surfaces, and Films*, 5 (6): 3313, 1987. doi: 10.1116/1.574189.
55. M. Schmid and P. Varga. Analysis of vibration-isolating systems for scanning tunneling microscopes. *Ultramicroscopy*, 42-44: 1610–1615, 1992. doi: 10.1016/0304-3991(92)90493-4.
56. D. L. Platus. Negative-stiffness-mechanism vibration isolation systems. *Proc. SPIE*, 3786 (July): 98–105, 1999. doi: 10.1117/12.363841.
57. Y. J. Song, A. F. Otte, V. Shvarts, Z. Zhao, Y. Kuk, S. R. Blankenship, A. Band, F. M. Hess, and J. Stroscio. Invited Review Article: A 10 mK scanning probe microscopy facility. *Review of Scientific Instruments*, 81 (12): 121101, 2010. doi: 10.1063/1.3520482.
58. A. Stalder and U. Duİˆrig. Ultrahigh vacuum compatible cooling and vibration isolation stage. *Review of Scientific Instruments*, 64: 3644, 1993.
59. P. Zahl, T. Wagner, R. Möller, and A. Klust. Open source scanning probe microscopy control software package GXSM. *Journal of Vacuum Science & Technology B: Microelectronics and Nanometer Structures*, 28 (3): C4E39, 2010. doi: 10.1116/1.3374719.
60. D. Clarke, M. Kroll, P. Kirchner, R. Cook, and B. Hockey. Amorphization and Conductivity of Silicon and Germanium Induced by Indentation. *Physical Review Letters*, 60 (21): 2156–2159, 1988. doi: 10.1103/PhysRevLett.60.2156.
61. D. J. Oliver, J. E. Bradby, S. Ruffell, J. S. Williams, and P. Munroe. Nanoindentation-induced phase transformation in relaxed and unrelaxed ion-implanted amorphous germanium. *Journal of Applied Physics*, 106 (9): 093509, 2009. doi: 10.1063/1.3255999.
62. O. Warren, S. Downs, and T. Wyrobek. Challenges and interesting observations associated with feedback-controlled nanoindentation. *Zeitschrift fur Metallkunde*, 95, 2004.
63. S. A. Joyce and J. E. Houston. A new force sensor force microscopy iincorporating control for interfacial. pages 710–715, 1991.
64. E. Lassner and W.-D. Schubert. Tungsten. 1999. doi: 10.1007/978-1-4615-4907-9.
65. E. W. Müller. Das Feldionenmikroskop. *Zeitschrift für Physik*, 131 (1): 136–142, 1951. doi: 10.1007/BF01329651.
66. T. T. Tsong. *Atom-probe field ion microscopy*. Cambridge University Press, New York, 1990.
67. M. K. Miller, A. Cerezo, M. G. Hetherington, and G. D. W. Smith. *Atom Probe Field Ion Microscopy*. Oxford University Press, 1996.
68. A. Schirmeisen, G. Cross, A. Stalder, P. H. Grütter, and U. Dürig. Metallic adhesion and tunnelling at the atomic scale. *New Journal of Physics*, 2: 1–10, 2000.
69. Y. Kuk and P. J. Silverman. Role of tip structure in scanning tunneling microscopy. *Applied Physics Letters*, 48 (23): 1597, 1986. doi: 10.1063/1.96828.
70. T. Sakurai, T. Hashizume, Y. Hasegawa, I. Kamiya, N. Sano, H. Yokoyama, H. Tanaka, I. Sumita, and S. Hyodo. New versatile room-temperature field ion scanning tunneling microscopy. *Journal of Vacuum Science & Technology A: Vacuum, Surfaces, and Films*, 8 (1): 324, 1990. doi: 10.1116/1.577098.
71. T. Sakurai, T. Hashizume, I. Kamiya, Y. Hasegawa, N. Sano, H. Pickering, and A. Sakai. Field ion-scanning tunneling microscopy. *Progress in Surface Science*, 33 (1): 3–89, 1990. doi: 10.1016/0079-6816(90)90012-9.
72. M. Tomitori, N. Hirano, F. Iwawaki, Y. Watanabe, T. Takayanagi, and O. Nishikawa. Elaboration and evaluation of tip manipulation of scanning tunneling microscopy. *Journal of Vacuum Science & Technology A: Vacuum, Surfaces, and Films*, 8 (1): 425, 1990. doi: 10.1116/1.576412.
73. M. Tomitori, K. Sugata, G. Okuyama, and H. Kimata. Reproducibility of scanning tunneling spectroscopy of Si(111)7 x 7 using a build-up tip. *Surface Science*, 355 (1-3): 21–30, 1996. doi: 10.1016/0039-6028(95)01377-6.
74. G. Cross, A. Schirmeisen, P. H. Grütter, A. Stalder, M. Tschudy, U. Dürig, and U. Duİˆrig. Adhesion Interaction between Atomically Defined Tip and Sample. *Physical Review Letters*, 80 (21): 4685–4688, 1998. doi: 10.1103/PhysRevLett.80.4685.
75. J. Falter, G. Langewisch, H. Hölscher, H. Fuchs, and a. Schirmeisen. Field ion microscopy characterized tips in noncontact atomic force microscopy: Quantification of long-range force interactions. *Physical Review B*, 87 (11): 115412, 2013. doi: 10.1103/PhysRevB.87.115412.
76. A. Fian, C. Ernst, and M. Leisch. Combined atom probe and STM study of tip-substrate interactions. *Fresenius' Journal of Analytical Chemistry*, 365 (1-3): 38–42, 1999. doi: 10.1007/s002160051441.
77. A. Fian and M. Leisch. Study on tip-substrate interactions by STM and APFIM. *Ultramicroscopy*, 95 (1-4): 189–197, 2003. doi: 10.1016/S0304-3991(02)00316-9.
78. U. Landman, W. D. Luedtke, N. A. Burnham, and R. J. Colton. Atomistic Mechanisms and Dynamics of Adhesion, Nanoindentation, and Fracture. *Science*, 248 (4954): 454–461, 1990. doi: 10.1126/science.248.4954.454.
79. O. Nishikawa and R. Walko. Field ion microscopical observation of twinning in iridium induced by a mechanical contact. *Acta Metallurgica*, 19 (11): 1163–1168, 1971. doi: 10.1016/0001-6160(71)90048-4.
80. T. Hagedorn, M. El Ouali, W. Paul, D. Oliver, Y. Miyahara, and P. H. Grütter. Refined tip preparation by electrochemical etching and ultrahigh vacuum treatment to obtain atomically sharp tips for scanning tunneling microscope and atomic force microscope. *Review of Scientific Instruments*, 82 (11): 113903, 2011. doi: 10.1063/1.3660279.
81. I. Ekvall, E. Wahlström, D. Claesson, H. k. Olin, and E. Olsson. Preparation and characterization of electrochemically etched W tips for STM. *Measurement Science and Technology*, 10 (1): 11–18, 1999. doi: 10.1088/0957-0233/10/1/006.
82. J. P. Ibe, P. P. Bey, S. L. Brandow, R. A. Brizzolara, N. A. Burnham, D. P. DiLella, R. J. Colton, K. P. Lee, and C. R. K. Marrian. On the electrochemical etching of tips for scanning tunneling microscopy. *Journal of Vacuum Science & Technology A: Vacuum, Surfaces, and Films*, 8 (4): 3570, 1990. doi: 10.1116/1.576509.
83. A. J. Melmed. The art and science and other aspects of making sharp tips. *Journal of Vacuum Science & Technology B: Microelectronics and Nanometer Structures*, 9 (2): 601, 1991. doi: 10.1116/1.585467.
84. A.-S. Lucier, H. Mortensen, Y. Sun, and P. H. Grütter. Determination of the atomic structure of scanning probe microscopy tungsten tips by field ion microscopy. *Physical Review B*, 72 (23): 235420, 2005. doi: 10.1103/PhysRevB.72.235420.
85. A.-S. Lucier. *Preparation and Characterization of Tungsten Tips Suitable for Molecular Electronics Studies*. Master's thesis, McGill University, 2004.
86. W. Paul, Y. Miyahara, and P. H. Grütter. Implementation of atomically defined field ion microscopy tips in scanning probe microscopy. *Nanotechnology*, 23 (33): 335702, 2012. doi: 10.1088/0957-4484/23/33/335702.
87. W. Paul and P. Grütter. Comment on 'Field ion microscopy characterized tips in noncontact atomic force microscopy: Quantification of long-range force interactions'. *arXiv:1304.6766*, 2013.
88. R. D. Webber, J. M. Walls, and R. Smith. Ring counting in field-ion micrographs. *Journal of Microscopy*, 113 (3): 291–299, 1978. doi: 10.1111/j.1365-2818.1978.tb00107.x.
89. R. D. Webber and J. M. Walls. The shape of field-ion emitters. *Journal of Physics D: Applied Physics*, 12 (9): 1589–1595, 1979. doi: 10.1088/0022-3727/12/9/021.
90. A. C. Fischer-Cripps. *Introduction to Contact Mechanics*. Mechanical Engineering Series. Springer, Boston, 2007. ISBN 978-0-387-68187-0. doi: 10.1007/978-0-387-68188-7. URL http://-www.springerlink.com/index/10.1007/978-0-387-68188-7.
91. K. L. Johnson. *Contact Mechanics*. Cambridge University Press, New York, 1996.
92. M. P. Allen. Introduction to Molecular Dynamics Simulation. In N. Attig, K. Binder, H. Grubmüller, and K. Kremer, editors, *Computational soft matter: from synthetic polymers to proteins*,

volume 23, pages 1–28. John von Neumann Institute for Computing, Jülich, 2004. ISBN 3000126414.
93. M. S. Daw, S. M. Foiles, and M. I. Baskes. The embedded-atom method: a review of theory and applications. *Materials Science Reports*, 9 (7-8): 251–310, 1993. doi: 10.1016/0920-2307(93)90001-U.
94. F. H. Stillinger and T. A. Weber. Computer simulation of local order in condensed phases of silicon. *Physical Review B*, 31 (8): 5262–5271, 1985. doi: 10.1103/PhysRevB.31.5262.
95. G. Grochola, S. P. Russo, and I. K. Snook. On fitting a gold embedded atom method potential using the force matching method. *The Journal of chemical physics*, 123 (20): 204719, 2005. doi: 10.1063/1.2124667.
96. D. Hull and D. J. Bacon. *Introduction to Dislocations*. Elsevier, New York, 5th edition, 2011. ISBN 9780080966724.
97. J. R. Morris, H. Bei, G. M. Pharr, and E. P. George. Size Effects and Stochastic Behavior of Nanoindentation Pop In. *Physical Review Letters*, 106 (16): 165502, 2011. doi: 10.1103/PhysRevLett.106.165502.
98. C. Kelchner, S. Plimpton, and J. Hamilton. Dislocation nucleation and defect structure during surface indentation. *Physical Review B*, 58 (17): 11085–11088, 1998. doi: 10.1103/PhysRevB.58.11085.
99. J. Li, K. J. Van Vliet, T. Zhu, S. Yip, and S. Suresh. Atomistic mechanisms governing elastic limit and incipient plasticity in crystals. *Nature*, 418 (6895): 307–10, 2002. doi: 10.1038/nature00865.
100. K. Van Vliet, J. Li, T. Zhu, S. Yip, and S. Suresh. Quantifying the early stages of plasticity through nanoscale experiments and simulations. *Physical Review B*, 67 (10): 1–15, 2003. doi: 10.1103/PhysRevB.67.104105.
101. T. Zhu, J. Li, K. J. Van Vliet, S. Ogata, S. Yip, and S. Suresh. Predictive modeling of nanoindentation-induced homogeneous dislocation nucleation in copper. *Journal of the Mechanics and Physics of Solids*, 52 (3): 691–724, 2004. doi: 10.1016/j.jmps.2003.07.006.
102. R. J. Wagner, L. Ma, F. Tavazza, and L. E. Levine. Dislocation nucleation during nanoindentation of aluminum. *Journal of Applied Physics*, 104 (11): 114311, 2008. doi: 10.1063/1.3021305.
103. C. A. Schuh, J. K. Mason, and A. C. Lund. Quantitative insight into dislocation nucleation from high-temperature nanoindentation experiments. *Nat Mater*, 4 (8): 617–621, 2005. doi: 10.1038/nmat1429.
104. C. Shin, Y. N. Osetsky, and R. E. Stoller. Dislocation nucleation and defect formation in copper by stepped spherical indenter. *Philosophical Magazine*, 92 (25-27): 3158–3171, 2012. doi: 10.1080/14786435.2012.682177.
105. V. Navarro, O. R. de La Fuente, A. Mascaraque, J. M. Rojo, and O. R. de la Fuente. Uncommon Dislocation Processes at the Incipient Plasticity of Stepped Gold Surfaces. *Physical Review Letters*, 100 (10): 105504, 2008. doi: 10.1103/PhysRevLett.100.105504.
106. J. A. Zimmerman, C. L. Kelchner, P. A. Klein, J. C. Hamilton, and S. M. Foiles. Surface Step Effects on Nanoindentation. *Physical Review Letters*, 87 (16): 165507, 2001. doi: 10.1103/PhysRevLett.87.165507.
107. J. Mason, A. Lund, and C. A. Schuh. Determining the activation energy and volume for the onset of plasticity during nanoindentation. *Physical Review B*, 73 (5): 1–14, 2006. doi: 10.1103/PhysRevB.73.054102.
108. B. Luan and M. O. Robbins. The breakdown of continuum models for mechanical contacts. *Nature*, 435 (7044): 929–32, 2005. doi: 10.1038/nature03700.
109. C. A. Schuh and A. C. Lund. Application of nucleation theory to the rate dependence of incipient plasticity during nanoindentation. *Journal of Materials Research*, 19 (07): 2152–2158, 2004. doi: 10.1557/JMR.2004.0276.
110. P. Egberts, R. Gralla, and R. Bennewitz. Temporal development of indentation plasticity on the atomic scale revealed by force microscopy. *Physical Review B*, 86 (3): 035446, 2012. doi: 10.1103/PhysRevB.86.035446.
111. S. a. Syed Asif and J. B. Pethica. Nanoindentation creep of single-crystal tungsten and gallium arsenide. *Philosophical Magazine A*, 76 (6): 1105–1118, 1997. doi: 10.1080/01418619708214217.
112. G. Feng and A. Ngan. Creep and strain burst in indium and aluminium during nanoindentation. *Scripta Materialia*, 45 (8): 971–976, 2001. doi: 10.1016/S1359-6462(01)01120-4.
113. B. N. Lucas and W. C. Oliver. Indentation power-law creep of high-purity indium. *Metallurgical and Materials Transactions A*, 30 (3): 601–610, 1999. doi: 10.1007/s11661-999-0051-7.
114. J. B. Adams, L. G. Hector, D. J. Siegel, H. Yu, and J. Zhong. Adhesion, lubrication and wear on the atomic scale. *Surface and Interface Analysis*, 31 (7): 619–626, 2001. doi: 10.1002/sia.1089.
115. J. Hagelaar, E. Bitzek, C. Flipse, and P. Gumbsch. Atomistic simulations of the formation and destruction of nanoindentation contacts in tungsten. *Physical Review B*, 73 (4): 045425, 2006. doi: 10.1103/PhysRevB.73.045425.
116. J. Song and D. Srolovitz. Atomistic simulation of multicycle asperity contact. *Acta Materialia*, 55 (14): 4759–4768, 2007. doi: 10.1016/j.actamat.2007.04.042.
117. A. Fortini, M. I. Mendelev, S. Buldyrev, and D. Srolovitz. Asperity contacts at the nanoscale: Comparison of Ru and Au. *Journal of Applied Physics*, 104 (7): 074320, 2008. doi: 10.1063/1.2991301.
118. D. J. Oliver, W. Paul, M. El Ouali, T. Hagedorn, Y. Miyahara, Y. Qi, and P. H. Grütter. One-to-one spatially matched experiment and atomistic simulations of nanometre-scale indentation. *Nanotechnology*, 25 (2): 025701, 2014. doi: 10.1088/0957-4484/25/2/025701.
119. W. Paul, D. Oliver, Y. Miyahara, and P. Grütter. Transient adhesion and conductance phenomena in initial nanoscale mechanical contacts between dissimilar metals. *Nanotechnology*, 24 (47): 475704, 2013. doi: 10.1088/0957-4484/24/47/475704.
120. N. Gosvami, M. Feldmann, J. Peguiron, M. Moseler, A. Schirmeisen, and R. Bennewitz. Ageing of a Microscopic Sliding Gold Contact at Low Temperatures. *Physical Review Letters*, 107 (14): 144303, 2011. doi: 10.1103/PhysRevLett.107.144303.
121. G. S. Rohrer. *Structure and Bonding in Crystalline Materials*. Cambridge University Press, New York, 2001.
122. M. Mishra, P. Egberts, R. Bennewitz, and I. Szlufarska. Friction model for single-asperity elastic-plastic contacts. *Physical Review B*, 86 (4): 045452, 2012. doi: 10.1103/PhysRevB.86.045452.
123. Q. Li, Y. Dong, D. Perez, A. Martini, and R. Carpick. Speed Dependence of Atomic Stick-Slip Friction in Optimally Matched Experiments and Molecular Dynamics Simulations. *Physical Review Letters*, 106 (12): 1–4, 2011. doi: 10.1103/PhysRevLett.106.126101.
124. Y. Dong, X. Z. Liu, P. Egberts, Z. Ye, R. W. Carpick, and A. Martini. Correlation Between Probe Shape and Atomic Friction Peaks at Graphite Step Edges. *Tribology Letters*, 50 (1): 49–57, 2012. doi: 10.1007/s11249-012-0072-z.
125. R. Bennewitz. Friction force microscopy. *Materials Today*, 8 (5): 42–48, 2005. doi: 10.1016/S1369-7021(05)00845-X.
126. A. Labuda, W. Paul, B. Pietrobon, R. B. Lennox, P. H. Grütter, and R. Bennewitz. High-resolution friction force microscopy under electrochemical control. *Review of Scientific Instruments*, 81 (8): 083701, 2010. doi: 10.1063/1.3470107.
127. J. Li, S. Sarkar, W. T. Cox, T. J. Lenosky, E. Bitzek, and Y. Wang. Diffusive molecular dynamics and its application to nanoindentation and sintering. *Physical Review B*, 84 (5): 054103, 2011. doi: 10.1103/PhysRevB.84.054103.
128. G. Henkelman and H. Jonsson. Long time scale kinetic Monte Carlo simulations without lattice approximation and predefined event table. *The Journal of Chemical Physics*, 115 (21): 9657, 2001. doi: 10.1063/1.1415500.
129. Y. V. Sharvin. A Possible Method for Studying Fermi Surfaces. *Journal of Experimental and Theoretical Physics*, 21: 655, 1965.
130. R. Landauer. Spatial Variation of Currents and Fields Due to Localized Scatterers in Metallic Conduction. *IBM Journal of Research and Development*, 1 (3): 223–231, 1957. doi: 10.1147/rd.13.0223.
131. M. Buttiker. Coherent and sequential tunneling in series barriers. *IBM Journal of Research and Development*, 32 (1): 63–75, 1988. doi: 10.1147/rd.321.0063.
132. B. van Wees, H. van Houten, C. Beenakker, J. Williamson, L. Kouwenhoven, D. van der Marel, and C. Foxon. Quantized conductance of point contacts in a two-dimensional electron gas. *Physical Review Letters*, 60 (9): 848–850, 1988. doi: 10.1103/PhysRevLett.60.848.

133. D. A. Wharam, T. J. Thornton, R. Newbury, M. Pepper, H. Ahmed, J. E. F. Frost, D. G. Hasko, D. C. Peacock, D. A. Ritchie, and G. A. C. Jones. One-dimensional transport and the quantisation of the ballistic resistance. *Journal of Physics C: Solid State Physics*, 21 (8): L209–L214, 1988. doi: 10.1088/0022-3719/21/8/002.
134. N. Agrat, A. Levy Yeyati, and J. M. van Ruitenbeek. Quantum properties of atomic-sized conductors. *Physics Reports*, 377 (2-3): 81–279, 2003. doi: 10.1016/S0370-1573(02)00633-6.
135. G. Rubio-Bollinger, N. Agrat, and P. Joyez. Metallic Adhesion in Atomic-Size Junctions. *Physical Review Letters*, 93 (11): 1–4, 2004. doi: 10.1103/PhysRevLett.93.116803.
136. van Ruitenbeek JM, J. Krans, C. Muller, I. Yanson, T. Govaert, and R. Hesper. One-atom point contacts. *Physical review. B, Condensed matter*, 48 (19): 14721–14724, 1993.
137. L. Olesen, E. Laegsgaard, I. Stensgaard, F. Besenbacher, J. Schiotz, P. Stoltze, K. Jacobsen, and J. No/rskov. Quantized conductance in an atom-sized point contact. *Physical Review Letters*, 72 (14): 2251–2254, 1994. doi: 10.1103/PhysRevLett.72.2251.
138. I. Yanson, O. Shklyarevskii, S. Csonka, H. van Kempen, S. Speller, a. Yanson, and J. van Ruitenbeek. Atomic-Size Oscillations in Conductance Histograms for Gold Nanowires and the Influence of Work Hardening. *Physical Review Letters*, 95 (25): 256806, 2005. doi: 10.1103/PhysRevLett.95.256806.
139. M. L. Trouwborst, E. H. Huisman, F. L. Bakker, S. J. van der Molen, and B. J. van Wees. Single Atom Adhesion in Optimized Gold Nanojunctions. *Physical Review Letters*, 100 (17): 1–4, 2008. doi: 10.1103/PhysRevLett.100.175502.
140. J. Kröger and H. Jensen. Conductance of tip-surface and tip-atom junctions on Au(111) explored by a scanning tunnelling microscope. *New Journal of Physics*, 9 (5): 153–153, 2007. doi: 10.1088/1367-2630/9/5/153.
141. J. Kröger, N. Néel, A. Sperl, Y. F. Wang, and R. Berndt. Single-atom contacts with a scanning tunnelling microscope. *New Journal of Physics*, 11 (12): 125006, 2009. doi: 10.1088/1367-2630/11/12/125006.
142. J. K. Gimzewski and R. Möller. Transition from the tunneling regime to point contact studied using scanning tunneling microscopy. *Physical review. B, Condensed matter*, 36 (2): 1284–1287, 1987.
143. D. Sánchez-Portal, C. Untiedt, J. M. Soler, N. Agrat, and J. J. Sáenz. Nanocontacts: Probing Electronic Structure under Extreme Uniaxial Strains. *Physical Review Letters*, 79 (21): 4198–4201, 1997. doi: 10.1103/PhysRevLett.79.4198.
144. L. Limot, R. Berndt, J. Kröger, W. A. Hofer, and a. Garcia-Lekue. Atom Transfer and Single-Adatom Contacts. *Physical Review Letters*, 94 (12): 1–4, 2005. doi: 10.1103/PhysRevLett.94.126102.
145. C. Sabater, C. Untiedt, J. J. Palacios, and M. J. Caturla. Mechanical Annealing of Metallic Electrodes at the Atomic Scale. *Physical Review Letters*, 108 (20): 205502, 2012. doi: 10.1103/PhysRevLett.108.205502.
146. T. Kizuka and H. Aoki. The Dynamics of Electromigration in Copper Nanocontacts. *Applied Physics Express*, 2: 075003, 2009. doi: 10.1143/APEX.2.075003.
147. H. Ohnishi, Y. Kondo, and K. Takayanagi. Quantized conductance through individual rows of suspended gold atoms. *Nature*, 395: 780, 1998. doi: 10.1038/27399.
148. Y. Kurui, Y. Oshima, M. Okamoto, and K. Takayanagi. Conductance quantization and dequantization in gold nanowires due to multiple reflection at the interface. *Physical Review B*, 79 (16): 165414, 2009. doi: 10.1103/PhysRevB.79.165414.
149. J. Kröger, N. Néel, and L. Limot. Contact to single atoms and molecules with the tip of a scanning tunnelling microscope. *Journal of Physics: Condensed Matter*, 20 (22): 223001, 2008. doi: 10.1088/0953-8984/20/22/223001.
150. D. J. Oliver, J. Maassen, M. El Ouali, W. Paul, T. Hagedorn, Y. Miyahara, Y. Qi, H. Guo, and P. H. Grütter. Conductivity of an atomically defined metallic interface. *Proceedings of the National Academy of Sciences of the United States of America*, 109 (47): 19097–102, 2012. doi: 10.1073/pnas.1208699109.
151. P. Muralt and D. W. Pohl. Scanning tunneling potentiometry. *Applied Physics Letters*, 48 (8): 514, 1986. doi: 10.1063/1.96491.
152. M. A. Schneider, M. Wenderoth, A. J. Heinrich, M. A. Rosentreter, and R. G. Ulbrich. Current transport through single grain boundaries: A scanning tunneling potentiometry study. *Applied Physics Letters*, 69 (9): 1327, 1996. doi: 10.1063/1.117583.
153. T.-H. Kim, X.-G. Zhang, D. M. Nicholson, B. M. Evans, N. S. Kulkarni, B. Radhakrishnan, E. a. Kenik, and A.-P. Li. Large discrete resistance jump at grain boundary in copper nanowire. *Nano letters*, 10 (8): 3096–100, 2010. doi: 10.1021/nl101734h.
154. K. W. Clark, X.-G. Zhang, I. V. Vlassiouk, G. He, R. M. Feenstra, and A.-P. Li. Spatially Resolved Mapping of Electrical Conductivity across Individual Domain (Grain) Boundaries in Graphene. *ACS nano*, (9): 7956–7966, 2013. doi: 10.1021/nn403056k.
155. B. Feldman, S. Park, M. Haverty, S. Shankar, and S. T. Dunham. Simulation of grain boundary effects on electronic transport in metals, and detailed causes of scattering. *Physica Status Solidi (B)*, 247 (7): 1791–1796, 2010. doi: 10.1002/pssb.201046133.
156. M. K. Srivastava, Y. Wang, X.-G. Zhang, D. M. C. Nicholson, and H.-P. Cheng. Plane-wave transport method for low-symmetry lattices and its application. *Physical Review B*, 86 (7): 075134, 2012. doi: 10.1103/PhysRevB.86.075134.
157. B.-H. Zhou, Y. Xu, S. Wang, G. Zhou, and K. Xia. An ab initio investigation on boundary resistance for metallic grains. *Solid State Communications*, 150 (29-30): 1422–1424, 2010. doi: 10.1016/j.ssc.2010.04.015.
158. P. Xu, K. Xia, M. Zwierzycki, M. Talanana, and P. Kelly. Orientation-Dependent Transparency of Metallic Interfaces. *Physical Review Letters*, 96 (17): 176602, 2006. doi: 10.1103/PhysRevLett.96.176602.
159. H. Knoppe and E. Bauer. Ultrathin Au films on W(110): Epitaxial growth and electronic structure. *Physical Review B*, 48 (8): 5621–5629, 1993. doi: 10.1103/PhysRevB.48.5621.
160. M. Rezeq, J. Pitters, and R. Wolkow. Tungsten nanotip fabrication by spatially controlled field-assisted reaction with nitrogen. *The Journal of Chemical Physics*, 124 (20): 204716, 2006. doi: 10.1063/1.2198536.
161. M. Rezeq, C. Joachim, and N. Chandrasekhar. Nanotip apex modification with atomic precision and single atom tips restoration. *Microelectronic Engineering*, 86 (4-6): 996–998, 2009. doi: 10.1016/j.mee.2008.10.022.
162. R. Urban, R. A. Wolkow, and J. L. Pitters. Field ion microscope evaluation of tungsten nanotip shape using He and Ne imaging gases. *Ultramicroscopy*, 122: 60–4, 2012. doi: 10.1016/j.ultramic.2012.07.026.
163. F. Rahman, J. Onoda, K. Imaizumi, and S. Mizuno. Field-assisted oxygen etching for sharp field-emission tip. *Surface Science*, 602 (12): 2128–2134, 2008. doi: 10.1016/j.susc.2008.04.034.
164. Y. Kobayashi, S. Yasuhiko, Y. Morikawa, K. Kajiwara, and K. Hata. Nanostructure formation onto a tip of field gas ion emitter by field-assisted oxygen etching. *Surface and Interface Analysis*, 42 (10-11): 1544–1547, 2010. doi: 10.1002/sia.3612.
165. C.-C. Chang, H.-S. Kuo, T. T. Tsong, and I.-S. Hwang. A fully coherent electron beam from a noble-metal covered W(111) single-atom emitter. *Nanotechnology*, 20 (11): 115401, 2009. doi: 10.1088/0957-4484/20/11/115401.
166. H.-S. Kuo, I.-S. Hwang, T.-Y. Fu, Y.-C. Lin, C.-C. Chang, and T. T. Tsong. Noble Metal/W(111) Single-Atom Tips and Their Field Electron and Ion Emission Characteristics. *Japanese Journal of Applied Physics*, 45 (No. 11): 8972–8983, 2006. doi: 10.1143/JJAP.45.8972.
167. T.-Y. Fu, Y.-C. Lin, H.-S. Kuo, I.-S. Hwang, and T. T. Tsong. Study of two types of Ir or Rh covered single atom pyramidal W tips. *Surface Science*, 601 (18): 3992–3995, 2007. doi: 10.1016/j.susc.2007.04.043.
168. H.-S. Kuo, I.-S. Hwang, T.-Y. Fu, Y.-H. Lu, C.-Y. Lin, and T. T. Tsong. Gas field ion source from an Ir/W<111> single-atom tip. *Applied Physics Letters*, 92 (6): 063106, 2008. doi: 10.1063/1.2844851.
169. I.-S. Hwang, H.-S. Kuo, C.-C. Chang, and T. T. Tsong. Noble-Metal Covered W(111) Single-Atom Electron Sources. *Journal of The Electrochemical Society*, 157 (2): P7, 2010. doi: 10.1149/1.3269925.
170. H.-S. Kuo, I.-S. Hwang, T.-Y. Fu, Y.-S. Hwang, Y.-H. Lu, C.-Y. Lin, T. T. Tsong, and J.-L. Hou. A single-atom sharp iridium tip as an emitter of gas field ion sources. *Nanotechnology*, 20 (33): 335701, 2009. doi: 10.1088/0957-4484/20/33/335701.

171. A. Golubok, S. Masalov, and N. Tarasov. Thermofield tip formation in UHV/STM combined with field-emission microscope. *Ultramicroscopy*, 42-44: 1574–1579, 1992. doi: 10.1016/0304-3991(92)90486-4.
172. V. G. Pavlov. Field-Desorption Microscopy Study of the Deformation of a Tungsten Tip Subjected to Thermal Treatment in an Electric Field. *Physics of the Solid State*, 47 (11): 2180, 2005. doi: 10.1134/1.2131165.
173. V. G. Pavlov. Variations in shapes of outgrowths on a tungsten tip during growth in an electric field. *Physics of the Solid State*, 48 (5): 969–972, 2006. doi: 10.1134/S1063783406050258.
174. V. G. Pavlov. Atomically sharp <111> trihedral angle of a tungsten tip. *Physics of the Solid State*, 49 (8): 1579–1582, 2007. doi: 10.1134/S1063783407080306.
175. N. Ohmae, M. Umeno, and K. Tsubouchi. Effect of Oxygen Adsorption on Adhesion of W to Au Studied by Field Ion Microscopy. *A S L E Transactions*, 30 (3): 409–418, 1987. doi: 10.1080/05698198708981774.
176. A. M. C. Valkering, A. I. Mares, C. Untiedt, K. B. Gavan, T. H. Oosterkamp, and J. M. van Ruitenbeek. A force sensor for atomic point contacts. *Review of Scientific Instruments*, 76 (10): 103903, 2005. doi: 10.1063/1.2084347.
177. J. Armstrong, S. Hua, and H. Chopra. Mechanics of quantum and Sharvin conductors. *Physical Review B*, 83 (23): 1–8, 2011. doi: 10.1103/PhysRevB.83.235422.